Sedimentary Geology 455 (2023) 106481

Contents lists available at ScienceDirect

Sedimentary Geology

journal homepage: www.elsevier.com/locate/sedgeo

Ediacaran cap carbonates with microbial build-ups capping barite-bearing methane seep networks in the Kaarta Mountains, Taoudeni Basin, Mali

J. Javier Álvaro [a,*], Kjell Billström [b], Christian Hallmann [c], Yosuke Hoshino [c], Alberto Jorge [d]

[a] Instituto de Geociencias (CSIC-UCM), Dr. Severo Ochoa 7, 28040 Madrid, Spain
[b] Department of Geological Sciences, Swedish Museum of Natural History, SE-104 05 Stockholm, Sweden
[c] GFZ German Research Center for Geosciences, Telegrafenberg, 14473 Potsdam, Germany
[d] Museo Nacional de Ciencias Naturales (CSIC), José Gutiérrez Abascal 2, 28006 Madrid, Spain

ARTICLE INFO

Article history:
Received 27 June 2023
Received in revised form 28 July 2023
Accepted 28 July 2023
Available online 06 August 2023

Editor: Dr. Brian Jones

Keywords:
Stromatolite
Isotope geochemistry
Stigmastanoid biomarker
Methane
Marinoan
Taoudeni Basin

ABSTRACT

Defining the variability and distribution of methane seeps and microbial activity in the aftermath of the Marinoan glaciation is a long-standing challenge in the field of Snowball models. Early diagenetic barite is commonly linked to tepee structures and associated breccias lacking microbial textures and fabrics, giving the impression that chemosynthetic microbes, or at least methane-tolerant microbes, did not participate in the carbonate production of their cap carbonate host. This apparent paradox has been an outstanding question in the lowermost Ediacaran cap carbonates of the Taoudeni Basin, NW Africa. In the Kaarta Mountains of Mali these carbonates exhibit, over short distances (<10 km), sharp facies-related environmental modifications with quiescent-dominated seafloor conditions, episodically interrupted by metre-scale disrupted substrates. The latter comprises fissure and fracture networks, occluded with tabular- and rosette-shaped barite cements, and sealed by decimetre-scale stromatolitic build-ups exhibiting intergrowths with barite needles. The strongly ^{13}C-depleted carbon isotope values of the microbial carbonates ($\delta^{13}C$ as low as −43.2 ‰ PDB) suggest the influence of methane, also preserved as fluid inclusions in barite crystals (documented with RAMAN spectroscopy) derived from a gas reservoir below the cap carbonate. T_h of other fluid inclusions (Linkam microthermometry), ranging from 174 °C to 222 °C, provides minimum entrapment temperatures for barite precipitation. The microbially induced oxidation of methane and input of Ba-rich fluids were coupled to reduction of sulphate derived from seawater. The Sr/S isotope ratio and barite shape and size point to diagenetic barite crystals. The biomarkers yielded by the cap carbonate reflect a C_{29}-dominant steroidal signature characteristic of stigmastanoid algal blooms. Although present-day microbial build-ups related to methane sources commonly occur in deep substrates and under anoxic bottom waters, the cap carbonate of the Kaarta Mountains is representative of shallower substrates, whereas its biomarkers point to deposition under episodic non-oxidising conditions.

1. Introduction

Methane seeps are commonly rich in chemosynthetic microbes forming biofilms, microbial mats and, in some cases, metre-scale build-ups named "chemoherms" (Aharon, 1994). Because methane fluxes can be enriched in Ba, the introduction of dissolved Ba^{2+} from methane can lead to precipitation of barite as cavity and fracture fills, and as sealing beds within sediments surrounding methane seep fields (Gill et al., 2005). Criteria to identify modern and ancient methane seeps that are associated with chemoautotrophic and methane-tolerant microbes include, amongst others: (i) mud volcanoes and diapirs, chimneys and pockmarks colonised by chemosynthetic microbes, and methane gas and fluid disruption associated with fissuring and brecciation; (ii) abundant solution cavities and fractures; (iii) carbonate crusts as well as cavity- and fracture-filling authigenic carbonate cements that record extreme $\delta^{13}C$ variability, with values ranging from >−50 ‰ to +6 ‰; (iv) framboidal pyrites with depleted $\delta^{34}S$ up to −46 ‰, lower than coexisting sulphates; and (v) local nucleation of barite deposits yielding both laterally continuous crusts, and infilling voids and porosities of tepee-like structures and sheet-cracks (e.g., Kennedy, 1996; Jiang et al., 2003, 2006a, 2006b; Campbell, 2006; Hoffman and Halverson, 2011; Okubo et al., 2020).

* Corresponding author.
E-mail addresses: jj.alvaro@csic.es (J.J. Álvaro), kjell.billstrom@nrm.se (K. Billström), challman@gfz-potsdam.de (C. Hallmann), yhoshino@gfz-potsdam.de (Y. Hoshino), alberto.jorge@aei.gob.es (A. Jorge).

https://doi.org/10.1016/j.sedgeo.2023.106481

A major destabilisation episode of equatorial permafrost methane clathrate is recorded in the lowermost Ediacaran cap carbonates, which would have influenced postglacial warming and oceanic oxygen level, considered as one of the triggering factors that controlled metazoan evolution preceding the Cambrian Explosion (Kirschvink and Raub, 2003; Kennedy et al., 2008). In Australia, California, Namibia, South China and NW Africa, some distinct features of these cap carbonates (e.g., sheet cracks, tube structures, tepee-like structures, barite fans, negative carbon isotope values, and associated fractures and cavities) have been interpreted as the result of gas and fluid escape associated with gas-hydrate destabilisation triggered by marine transgression and warming after the Marinoan glaciation (Jiang et al., 2003, 2006a, 2006b; Shields et al., 2007a; Kennedy et al., 2008; Peng et al., 2011; Sato et al., 2016; Zhao et al., 2021). However, microbial textures and fabrics associated with these cold seepages are largely absent, giving the impression that chemosynthetic microbes, or at least methane-tolerant microbes, did not participate in the carbonate production of cap carbonates. The aim of this paper is to document the nucleation and growth of microbial build-ups (or chemoherms) forming metre-scale haloes capping some methane-barite seep fields in the Taoudeni Basin using a targeted, multi-proxy approach. Additional issues include the source of the sulphur and strontium in the barites, the fluid-flow forcing mechanisms leading to the onset of disrupted substrates, and the microbial role and diagenetic overprint in the development of cap carbonate build-ups in the aftermath of the Marinoan Snowball glaciation.

2. Geological setting and stratigraphy

The West African craton is surrounded by several Upper Proterozoic–Palaeozoic fold belts. The Archean (~2500 Ma) and Birrimian (2000–1700 Ma) basement of the craton mainly crops out along the Reguibat and Leo Shields, although scattered inliers are also exposed along the Bassaride and Mauritanide belts, and the core of the Anti-Atlas belt (Fig. 1A). The cratonic sedimentary cover configures the Taoudeni Basin. Its infill ranges from Proterozoic (ca. 1100 Ma; Rooney et al., 2010) to Upper Carboniferous and reaches 2–3 km in average thickness. Three main tectono-thermal events structured the Taoudeni Basin: (i) the Pan-African I or Bassaride orogen (ca. 660–650 Ma); (ii) the Pan-African II or Rokelide orogen (550–530 Ma); and (iii) the Variscan orogen linked to the emplacement of internal nappes in the Mauritanide fold belt (330–270 Ma; Villeneuve, 2008). The Taoudeni Basin can be subdivided into eight different sub-basins or depocenters, from which the Adrar, Hohd and Hank sub-basins contain thick Neoproterozoic–Lower Palaeozoic strata (Villeneuve, 2005) (Fig. 1A).

Detailed lithostratigraphic subdivision and mapping of the Neoproterozoic glaciogenic 'triad' (tillite-cap carbonate-"silexite" or chert) throughout the Hohd sub-basin, on which this paper is focused, was summarised in Deynoux et al. (2006) (Fig. 2). Glaciogenic strata of the Koniakari (former Bakoye) Group were extensively studied, but the barite-bearing cap carbonate has only been studied in detail in the Adrar sub-basin (Álvaro et al., 2007; Shields et al., 2007a) and the Senegal/Guinea border (Shields et al., 2007b), where cavity- and fracture-fill barite mineralizations are seemingly unrelated to microbial activity. In this work, two sections have been measured in the Kaarta Mountains neighbouring Kayes city (Fig. 1B). Although they are relatively close to each other (<10 km far away), the same lowermost Ediacaran cap carbonate exhibits different facies associations and sedimentary structures. In the study area, the diamictite and cap carbonate units of the Koniakari Group, up to 100 m thick, are overlain by a chert package that marks the base of the Nioro Group, a heterolithic unit composed of chert and variegated shale (Deynoux et al., 2006).

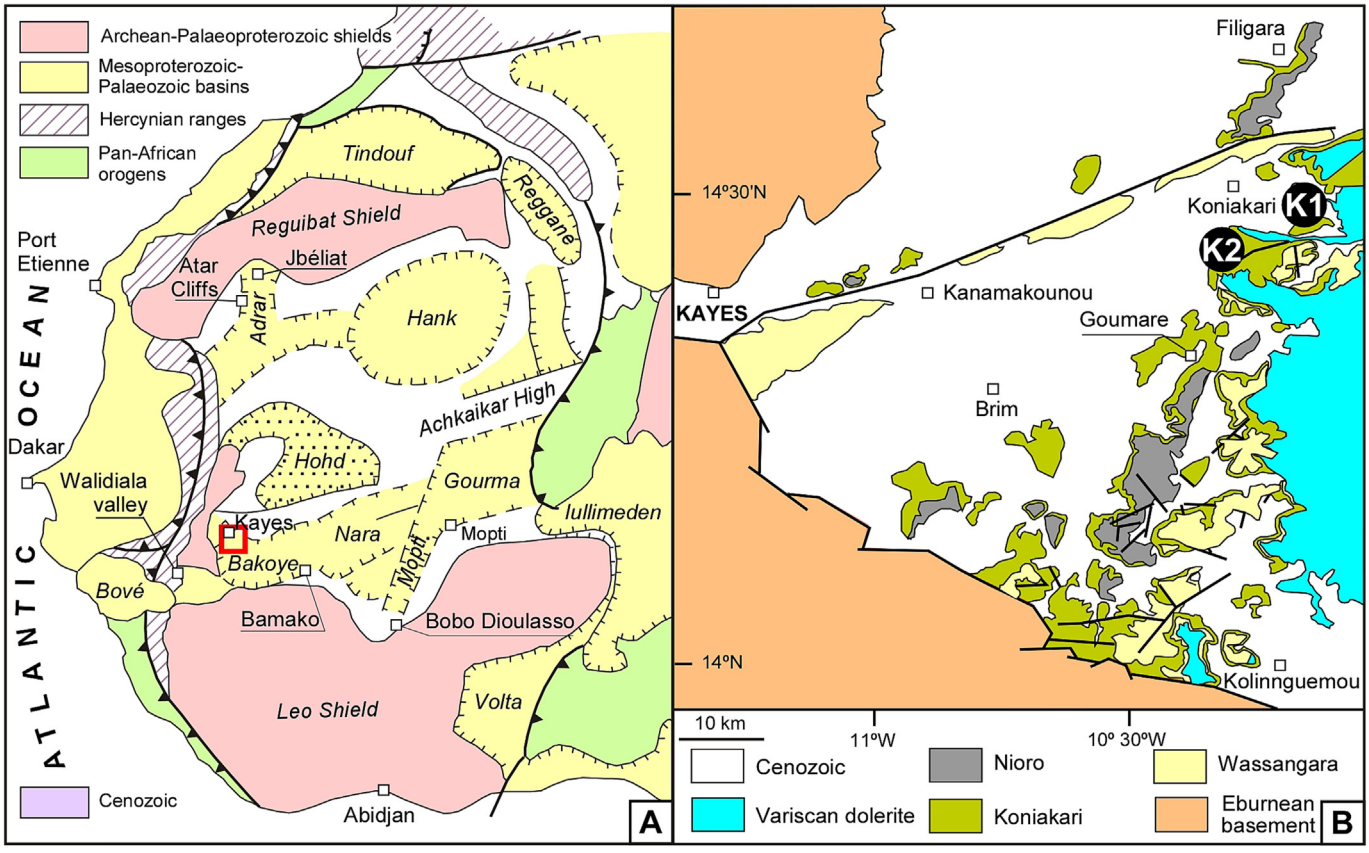

Fig. 1. A. Geological sketch of the West African craton; modified from Deynoux et al. (2006). B. Geological map of the Kaarta Mountains, western Mali, with setting of studied sections; modified from Bense (1964) and Rossi (1982).

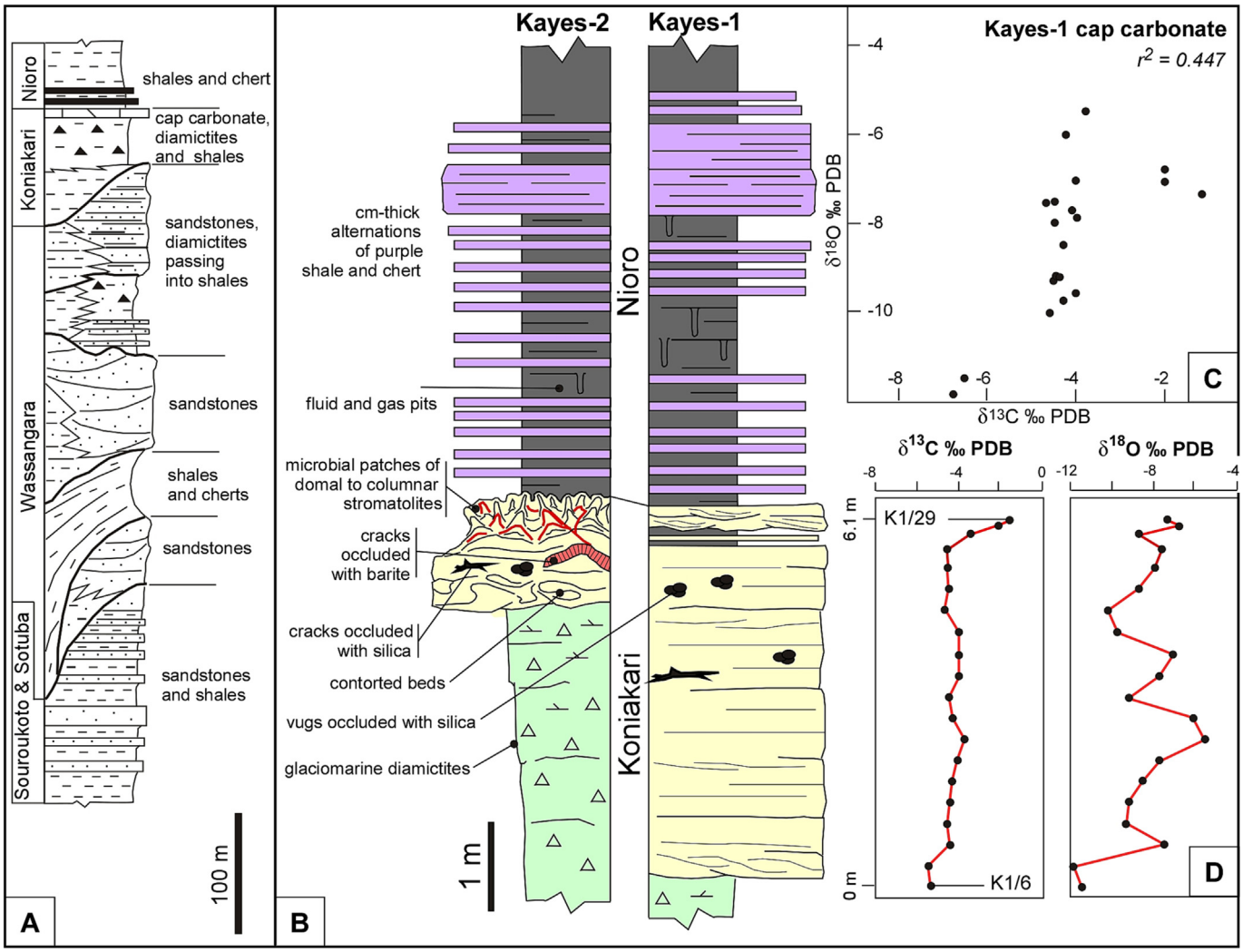

Fig. 2. A. Stratigraphic chart of the Neoproterozoic succession in the Mandingue and Tanbaoura plateaux and Kaarta Mountains, western Mali; modified from Deynoux et al. (2006). B. Stratigraphic logs of the Kayes-1 and Kayes-2 measured sections. C. Bivariate δ^{13}Ccarb vs. δ^{18}Ocarb plot of the chemostratigraphic data measured in section Kayes-1; r^2 = coefficient of correlation. D. Chemostratigraphic log of carbon and oxygen stable-isotope profiles from the Koniakari cap carbonate in section Kayes-1.

Deposition of the Neoproterozoic 'triad' throughout the Taoudeni Basin took place between the Bassaride (665–655 Ma) and Dahomeyide (610–580 Ma; Deynoux et al., 2006) orogens. As a result, the Koniakari cap carbonate is allocated to the end of the late Cryogenian (Marinoan) glaciation. This assignation fits with two confident U/Pb zircon ages yielded by the analysis of tuffites that overlie the cap carbonate in the Adrar of Mauritania and the Mauritanide Belt (Lahondère et al., 2005; Álvaro et al., 2007; Shields et al., 2007a).

3. Material and methods

About 120 samples from the Koniakari cap carbonate and the overlying Nioro chert from sections K1 and K2 (Figs. 1B, 2) were prepared for petrographic examination and geochemical sampling by polishing cut surfaces. To distinguish calcite from dolomite and to identify ferroan cements, carbonates were stained with Alizarin Red S and potassium ferricyanide. A binocular mounted dental drill allowed sampling of carbonate and barite components from chips and rock slabs.

Transmitted and reflected light microscopy, X-ray diffraction (XRD), scanning electron microscopy (SEM) equipped with an energy-dispersive X-ray analyser (EDX), and back-scattered electron detector (BSE) were used for mineralogical identification in the Museo Nacional de Ciencias Naturales (MNCN) and the Complutense University, Madrid. SEM analysis was made by using a JEOL JSM-6400 fitted with an Oxford Instruments D6679 detector. BSE imaging and energy-dispersive X-ray (EDS) analyses were obtained by SEM with accelerating voltage 20 kV, beam current 1–2 nÅ, and a counting interval of 50 s; analytical results display an error of ±5–7 %.

The petrographic and microthermometric studies of fluid inclusions on doubly polished thin-sections of barite were performed by using a Linkam stage (Linkam Scientific, Tadworth, UK) fitted on a binocular Olympus BX51 microscope (Olympus, Tokyo, Japan). The microthermometric study was performed in a Linkam THMSG-600 heating and freezing stage (Linkam Scientific). The fluid inclusion assemblage approach of Goldstein and Reynolds (1994) was followed. The non-intrusive and non-destructive Raman spectroscopy technique (confocal Raman microscopy Thermo Fischer DXR spectrograph, Verona Road Madison, WI 53711-4495, USA) of MNCN was used to characterise fluid inclusions, <2 μm in size, in barite crystals (see methodology in Frezzotti et al., 2012). The light at 532 nm of a frequency doubled Nd: YVO_4 DPSS solid laser (maximum power 30 mW) was used for excitation. The average spectral resolution in the Raman shift ranging from 200 to 3600 cm^{-1} was 4 cm^{-1}, i.e. grating 900 lines/mm and 2 μm spot sizes. Analysis was made at room temperature, as the peak position of CH_4 *L* (in liquid) increases continuously with temperature, from 2907 cm^{-1} at −5 °C to 2914 cm^{-1} at +25 °C (Beeskow et al., 2005).

$\delta^{34}S$ analysis of barite samples and $\delta^{13}C/\delta^{18}O$ analysis of carbonates were carried out at the Universities of Salamanca and Erlangen, respectively. Sulphur isotopic ratios in barite were obtained on SO_2 liberated by standard stable isotopic extraction techniques (Coleman and Moore, 1978), which were analysed in a dedicated SIRAII (VG Isogas) dual inlet mass spectrometer. The data are reported in the usual delta notation, relative to CDT ($^{34}S/^{32}S$). The overall reproducibility ($1\sigma = 3$) of the laboratory working standards was better than 0.27 ‰ for $\delta^{34}S$. Carbonate powders were reacted at 75° with 100 % phosphoric acid using a Kiel III carbonate preparation line connected to a Thermo-Finnigan 252 mass spectrometer. All values are reported in ‰ relative to V-PDB by assigning a $\delta^{13}C$ value of +1.95 ‰ and a $\delta^{18}O$ value of −2.20 ‰ to NBS19. The reproducibility was checked by replicate analyses of laboratory standards and is better than ±0.01–0.02 ‰.

Sr isotopic ratios were determined using a Thermo-Finnigan MAT 261 (TIMS) mass spectrometer at the Swedish Museum of Natural History, Stockholm. About 100 mg of finely ground barite was partly dissolved overnight in 6 N HCl at 100 °C. Subsequently, the undissolved material was taken up in a HF/HNO_3 mixture following the Teflon bomb method of Krogh (1973); and after 2 days in the oven at 205 °C, sample solutions were combined, centrifuged and evaporated to dryness. Finally, the samples were re-dissolved in 2.5 N HCl and Sr was isolated following standard ion exchange procedures. The $^{87}Sr/^{86}Sr$ isotope ratios, with a within-run error of ±0.000009 or less, were normalised to the SRM987standard value.

To allow for contamination control in biomarker analysis, samples were separated into interior and exterior portions by sawing or by micro-ablation. Solvent extraction was performed under ultrasound assisted agitation with dichloromethane (DCM) and fractionated into compound classes as described elsewhere (Hallmann et al., 2011; Hoshino et al., 2017). Molecular analyses (full scan) were performed on a Trace GC Ultra (Thermo Scientific) coupled to an ALMSCO BenchTOF-dx mass spectrometer. The GC was fitted with a VF-1 MS column (40 m × 0.15 mm × 0.15 μm) and operated with a constant flow (1.4 ml/min) of helium (99.999 % pure, Westfalen AG) as a carrier gas. Samples were injected in splitless mode using a PTV injector (60 °C to 315 °C at 14.5°/s). The GC oven was held at 60 °C (2 min), ramped at 4.5°/min to 325 °C and held for 10 min. Ionisation was achieved at 70 eV (electron impact) and 250 °C with a filament current of ca. 4 A. Data were measured from *m/z* 30 to 800 but only recorded from *m/z* 50 to 550 at ca. 1000 mass resolution using 2469 scans per scanset and a scanset period of 250 ms. Analytes were quantified by comparison to internal standards without correcting for individual response factors. Biomarker analysis (in MS/MS mode) was performed on a Thermo Quantum XLS Ultra triple-quadrupole mass spectrometer coupled to a Thermo Trace GC Ultra, fitted with a DB-XLB capillary column (60 m × 0.25 mm × 0.25 μm) and operated with a constant flow (1.3 ml/min) of helium (99.999 % pure, Westfalen AG). Volumes of typically 1 or 2 μl were injected on column at 70 °C. The oven was held isothermal at 70 °C (5 min), heated to 335 °C at 4°/min and held at the final temperature for 9 min. Ionisation was achieved by electron impact at 70 eV and 250 °C with an emission current of typically 50 μA. Q1 and Q3 were each operated in 0.7 Da resolution with a cycle time of 0.5 s. Q2 was operated with Argon 5.0 collision gas at a pressure of 1.1 mTorr and varying collision voltages depending on the target analyte. Compounds were quantified on characteristic parent-to-daughter ion mass transitions without correcting for differential response factors.

4. Cap carbonate deposited under quiescent conditions

We follow Deynoux et al.'s (2006) lithostratigraphic subdivision of the Cryogenian–Ediacaran transition in the Mandingue and Tanbaoura plateaux of western Mali into the Koniakari and Nioro groups, which directly onlap an exhumed Eburnean basement. The Koniakari Group consists of marine shales, diamictites and a cap carbonate conformably overlain by the Nioro Group, which begins with an alternation of chert and variegated shale. The following description fits the classical 'triad' on stable substrates (section K1; Figs. 1, 2).

4.1. Underlying diamictite (Koniakari Group)

The Koniakari diamictite consists of massive to poorly stratified, green to brownish shales with variable proportions (10–70 %) of randomly dispersed, angular to subrounded outsized clasts, isolated or chaotically clustered, ranging in size from silt to boulder and lacking any preferred long-axis alignment. Beds range from 10 cm to several metres in thickness. Crude layering is defined by variation in the percentage of detrital clasts (Fig. 3A). Clast composition is dominated by quartz, feldspar, quartzite and dolostone with peloidal/ooidal grainstone textures. Neither striated nor faceted clasts were observed, whereas convoluted and distorted bedding is locally present. Lonestones embedded within crudely laminated shales deformed the subjacent laminae by loading, whereas the overlying laminae occur onlapping and draping above such clasts.

4.2. Cap carbonate (Koniakari Group)

The cap carbonate can be informally subdivided into three partly dolomitized limestone beds (37.1, 0.2 and 0.6 m thick, respectively) separated by two interbeds of black shale (0.3 and 1.8 m thick; Fig. 2B). The base of each limestone bed is scoured and its lower part consists of a silty limestone displaying medium-scale sets, laterally truncated, of trough and low-angle cross-laminae (Fig. 3B). These structures are covered by finely laminated, micritic to microsparitic limestone. Laminae become subparallel (Fig. 3C), gently inclined and even undulating over lateral distances of <1 m. The upper part of the thickest limestone bed displays centimetre-scale tepee-like structures, solution vugs and sheet-cracks occluded with silica. Microlithic feldspar phenocrysts and mafic pseudomorphs are locally abundant.

4.3. Chert (Nioro Group)

The chert unit displays decimetre-scale bedding with a conspicuous parallel microlamination, locally highlighted by unsilicified shale interlaminae. Scattered bands of unsilicified shales, up to 2 cm thick, become abundant upsection, where silicification decreases gradually leading to the identification of chert/shale couplets (Fig. 3D). Chert beds consist of alternations of siliceous shale and millimetre- to centimetre-thick, graded chert displaying low-angle and small-scale cross-lamination and numerous siliciclastic grain pseudomorphs. The chert/shale contacts are sharp and currently scoured (Fig. 3E), providing that microstylolites are absent. Putative microbial pseudomorphs were observed in some finely silicified layers, and consist of three-dimensional meshworks with small (up to 300 μm long), straight and (un)branching filaments (Fig. 3F). "Tube rocks" or "tubestones" are recognised in shale interbeds. Two tubular structures were observed: (i) I-shaped vertical pipes, up to 5 cm long and with diameters <1 cm across (Fig. 3G); and (ii) hemispherical pits, circular in plan outline, with a bowl-shaped central depression (Fig. 3H, I). The latter display central pits are up to 1 cm deep and 4 cm in diameter, surrounded by hemispherical dome-like elevations raised 2–3 cm above the bedding surface; the edges of the domes grade into the surrounding sediment.

4.4. Palaeoenvironments

The Koniakari diamictite was reported as glaciomarine in previous works based on the presence of lonestones and outsized gravels interpretable as ice-rafted dropstones (Deynoux et al., 2006). The interpretation is also supported by the geometrical relationships of the outsized clasts and the crudely laminated host-rock, the clast size and the provenance of carbonate clasts. Some of them, displaying laminated and peloidal/ooidal grainstone textures, derived from the uppermost

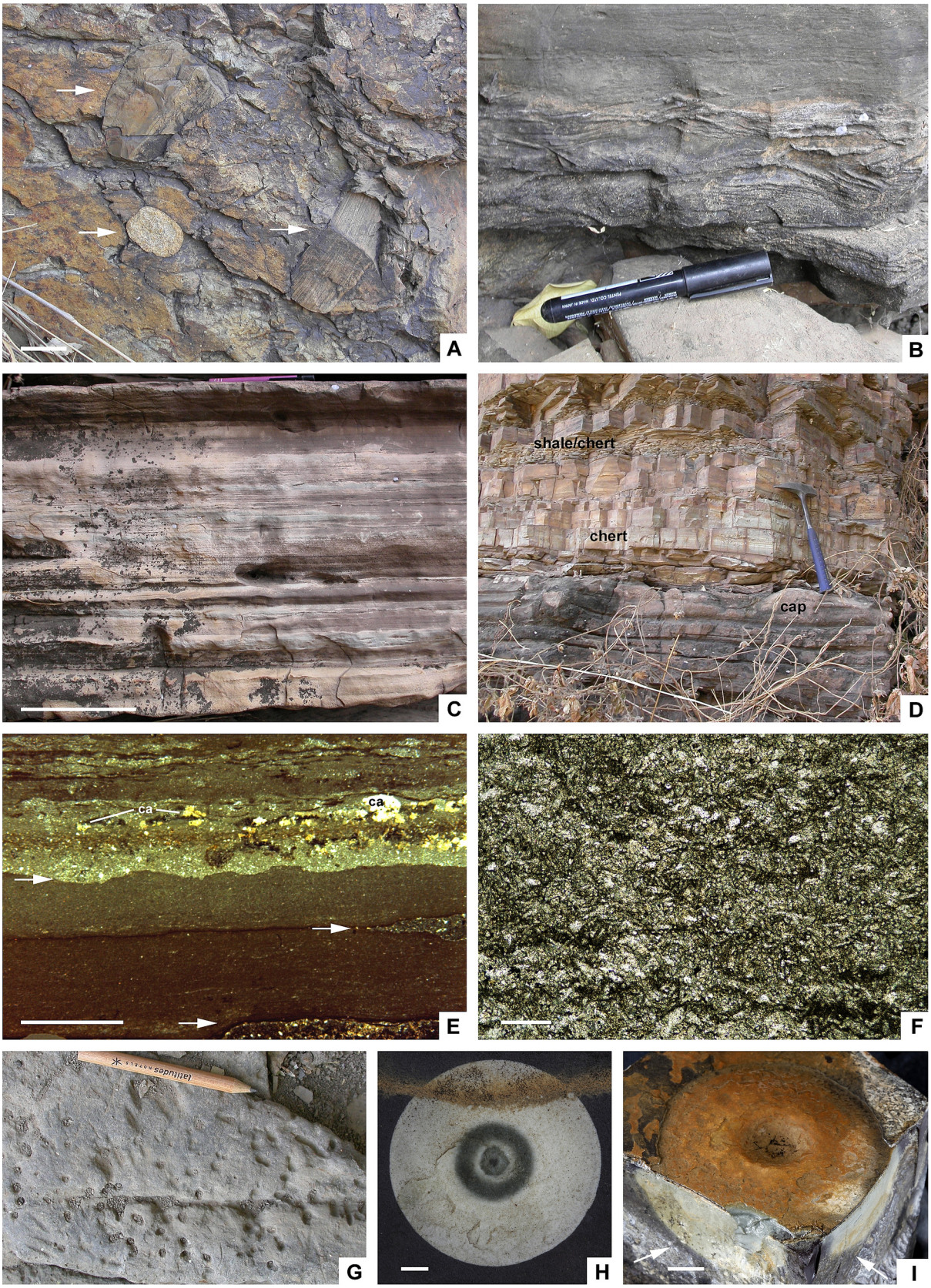

Fig. 3. Facies aspect of the Koniakari diamictite and cap carbonate and the Nioro chert at the Kayes–1 section. A. Massive diamictite disrupted by quartzite outsized lonestones (arrowed). B. Small-scale cross lamination crosscut by scoured surfaces marking the base of the cap carbonate. C. Millimetre- to centimetre-scale parallel lamination of cap carbonate. D. Cap carbonate/chert sharp contact showing the progressive upsection increase of shale interbeds in the Nioro chert. E. Millimetre-scale couplets of partly silicified shale and chert with arrows marking erosive contacts; ca = clasts of calcite. F. Meshwork of putative silicified microbial filaments. G. Bed surface from the lowermost Nioro chert punctuated by I-shaped fluid escape pipes. H. Bed surface with a bowl-shaped microbial gas pit with crater at its centre. I. 3D structure with longitudinal sections showing bowl-shaped depression of basal part (arrowed); scale bars = 4 cm (A), 15 (C), 2 mm (E), 200 μm (F), and 5 mm (H–I).

Mesoproterozoic Atar, Irma and Dimamou carbonates (Bertrand-Sarfati and Moussine-Pouchkine, 1983; Deynoux et al., 2006).

Each carbonate sub-unit of the Koniakari cap carbonate displays an upsection change from trough cross-stratified silty limestone to partly dolomitized limestone with low-angle planar cross-bedding and (mechanically laminated) subparallel-horizontal bedding punctuated with sheet cracks and pseudotepees. The vertical change of sedimentary structures reflects shoaling processes reaching peritidal environments, which were interrupted by drowning pulses and deposition of black shales. The latter marks the final flooding of the platform.

The grain size, normal grading separated by subparallel erosive bases, and average bed thickness displayed by the bedded chert and its upward transition into shale/chert alternations, suggest a clayey progenitor, which was subsequently silicified, formed by low density, silty, distal turbidity currents. The laterally persistence of the chert reflects predominant quiet substrates, episodically punctuated by distal turbiditic currents. Silicified pseudomorphs of filament meshworks reflect growth and decay of microbial biofilms and mats. I-shaped vertical pipes are commonly attributed to fluid or gas escape, and mimic those reported from the Marinoan cap carbonate of Namibia (Hoffman, 2011; Morris and Grotzinger, 2023). They differ from "tubestone microbialites" housed in stromatolitic carbonates from coeval cap carbonates in Death Valley and Brazil (Corsetti and Grotzinger, 2005; Romero et al., 2016). In contrast, bowl-shaped "tube rocks" probably represent fossil gas domes (microbial gas pits sensu Dragantis and Noffke, 2004), originated from gases generated and accumulated underneath sediment-sealing microbial mats. In this case, generation of gases may be related to decay of buried microbial biofilms and mats (Dornbos et al., 2007), preserved as silicified pseudomorphs of filament meshworks.

The sharp end of the Marinoan glaciation caused vast coastal flooding, as a result of which cap carbonate draped across continental margins and palaeotopographies as flooding progressed. Cap carbonates were deposited in a diachronous way, becoming younger with increasing palaeorelief elevation (Álvaro et al., 2007; Shields et al., 2007a); their geographical extent connotes an anomalous alkaline flux during deglaciation, in addition to strong surface warming (Hoffman and Macdonald, 2010). The cap carbonate and overlying chert found across the Taoudeni Basin are associated with deglacial to post-glacial eustatic transgression, respectively (Shields et al., 2007a). The end of carbonate production is marked by the establishment of background shale deposition, episodically interrupted by distal turbidites, and the definitive burial of an inherited palaeorelief, represented in the Kaarta Mountains by the Wassangara, Souroukoto and Sotuba basement (see Fig. 2). Carbonates also display accumulations of silt-sized pyroclastic ejecta (feldspar phenocrysts and mafic pseudomorphs) episodically derived from explosive felsic volcanism. Volcanism and deglaciation were roughly concurrent in the Taoudeni Basin, as previously recognised in the Mauritanides (Villeneuve, 2005), the Senegal/Guinea border (Shields et al., 2007b) and the Adrar of Mauritania (Álvaro et al., 2007).

5. Cap carbonate on disrupted substrates

The cap carbonate at section K2, 0.8–1.1 m thick, is fissured, convoluted and locally brecciated. Brittle and ductile arching gave way to fractured domed and bent structures, including upward buckling of fragmented blocks and overturned folds. The relative chronology of these processes can be assessed after determination of crosscutting relationships between hydrothermal mineralisation, fissuring networks, and laterally persistent, scoured discontinuities (D1 and D2 in Fig. 4A): (i) D1 separates a lower convoluted and deformed dolostone bed (30–40 cm thick) from an upper bedded and slightly deformed dolostone (30–40 cm thick); and (ii) the overlying D2 marks the base of a complex carbonate framework (20–30 cm thick) comprising deformed dolostone beds, convoluted and brecciated dolostone, microbial mat and stromatolite dolostones crosscut by barite dykes. The entire carbonate and vein network framework of the cap carbonate is sealed by the Nioro chert.

5.1. Facies associations

Underlying D1, the lower convoluted and deformed unit contains numerous shrinkage-like cracks. Centimetre-thick beds are chaotically arranged displaying synsedimentary bedding distortion and intraformational slumps affected by truncation surfaces (Fig. 4C, D). Cracks are commonly buckled, rarely parallel to bedding, and occluded with silica (see below for a detailed diagenetic description). Neptunian dykes are not recognised due to the lack of marine sediment filling open fissures and cracks. The middle unit, sandwiched between D1 and D2, shows ductile arching and boudinage (Fig. 4E). The upper unit, overlying D2, consists of deformed and convoluted beds hosting contorted barite dykes, capped by decimetre-scale, domal to columnar stromatolite patches flanked by flake breccia (stromatoclasts) (Figs. 4B, F, 5A–E). The stromatolites consist mainly of flat, planar crinkle laminae (maximum 3–5 mm thick), rich in fenestrae and locally affected by tepee-like structures, to domal boundstone finely laminated dolomicrosparite alternating with palisadic crystals of barite needles.

5.2. Palaeoenvironments

Soft-sediment deformation is represented by different types of contorted and folded structures related to downslope movements by basal sliding of semi-rigid to plastic sediment packages. The illustrated shrinkage cracks are similar to ptygmatic septarian cracks reported by Pratt (2001) and McMahon et al. (2016). Tepee-like structures are also similar to seismically generated structures (Pratt, 2002). The ductile arching and boudinage of the middle unit indicate the absence of brittle deformation and relative sediment cohesiveness. The coexistence of convoluted and rigid breccia fragments suggests active fracturing of both indurated and incompletely consolidated substrates. Localised fracturing episodes controlled by vertical tensile joints affected a semi-lithified carbonate host permitting upward injection of barium-related fluids. Mechanical behaviour of the host rock evolved in time, as lithification progressed, to more brittle conditions, as illustrated by cracking of the previously formed soft-sediment deformation structures. The lithification of the host rock was neither vertically uniform nor took place concurrently in the three interstratified beds that form the cap carbonate. Highly contorted dykes developed as a result of deformation preceding lithification of the host rock.

The veining and precipitation of barite as palisadic crystals filling dykes is only observed in the upper part, which suggests that the lower part was partly indurated when the dyke emplaced; isopachous layering of barite crystals is typical of chemical precipitates. The dykes occluded with barite were subsequently disrupted, via ductile deformation, by short-lived tensional episodes. At least, some of the barite mineralisation occurred contemporaneously with deposition of the microbial carbonate host. Encased barite-rich dykes show distinct crosscutting relationships with the host rock. The ends of highly contorted dykes terminate abruptly against discontinuity D2 (Fig. 4A). Barite occurs as palisadic crystals filling cracks, veins, and fractures; fracture (D2) is slightly older than the dyke.

6. Cap carbonate and chert diagenesis

A textural examination of the Koniakari cap carbonate and the Nioro chert on bedded and disrupted substrates has revealed striking evidence for repeated episodes of fracturation and solution, vein opening and resealing by subsequent cementation, yielding distinctive vein, crack and void complexes and crosscutting relationships. The paragenetic sequence of the cap carbonate (summarised in Fig. 6) can be subdivided into eight distinct precipitation episodes separated by, at least, four diagenetic fissuring/solution events. Three precipitation cements are exclusive of the disrupted cap carbonate (*ba1*, *si3* and

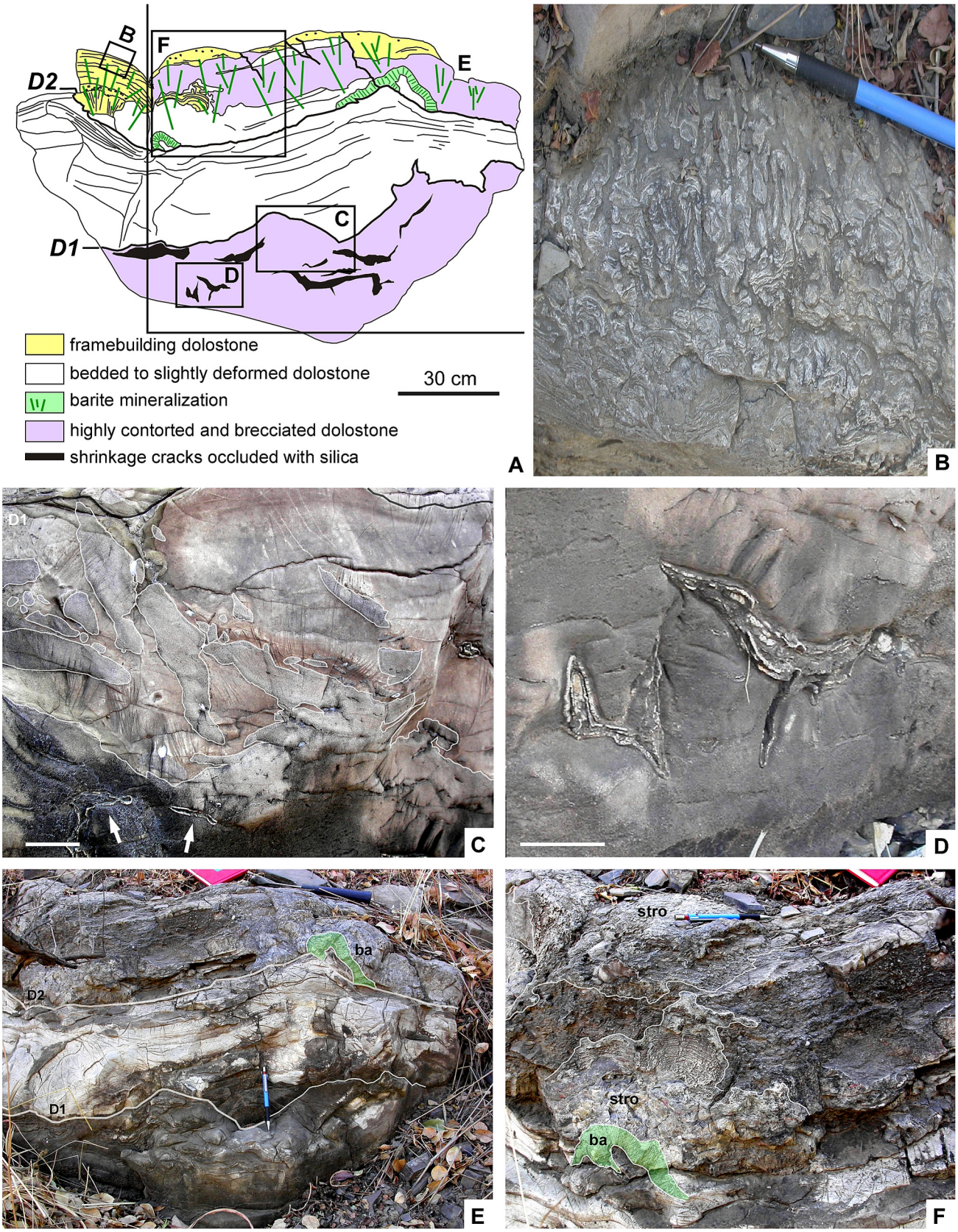

Fig. 4. Facies aspect of the disrupted cap carbonate at the Kayes-2 section. A. Sketch of exposure illustrating the three-fold bed differentiation bounded by discontinuities D1 and D2. B. Columnar stromatolitic dolostone marking the top of the cap carbonate. C. Contorted and fragmented, centimetre-thick, intraformational breccia capping shrinkage cracks (arrowed). D. Detail of shrinkage cracks. E–F. Detailed crosscutting relationships of D1, D2, barite dykes (*ba*, in green), and stromatolitic (stro) patches; scale bars = 3 cm (C), and 2 cm (D).

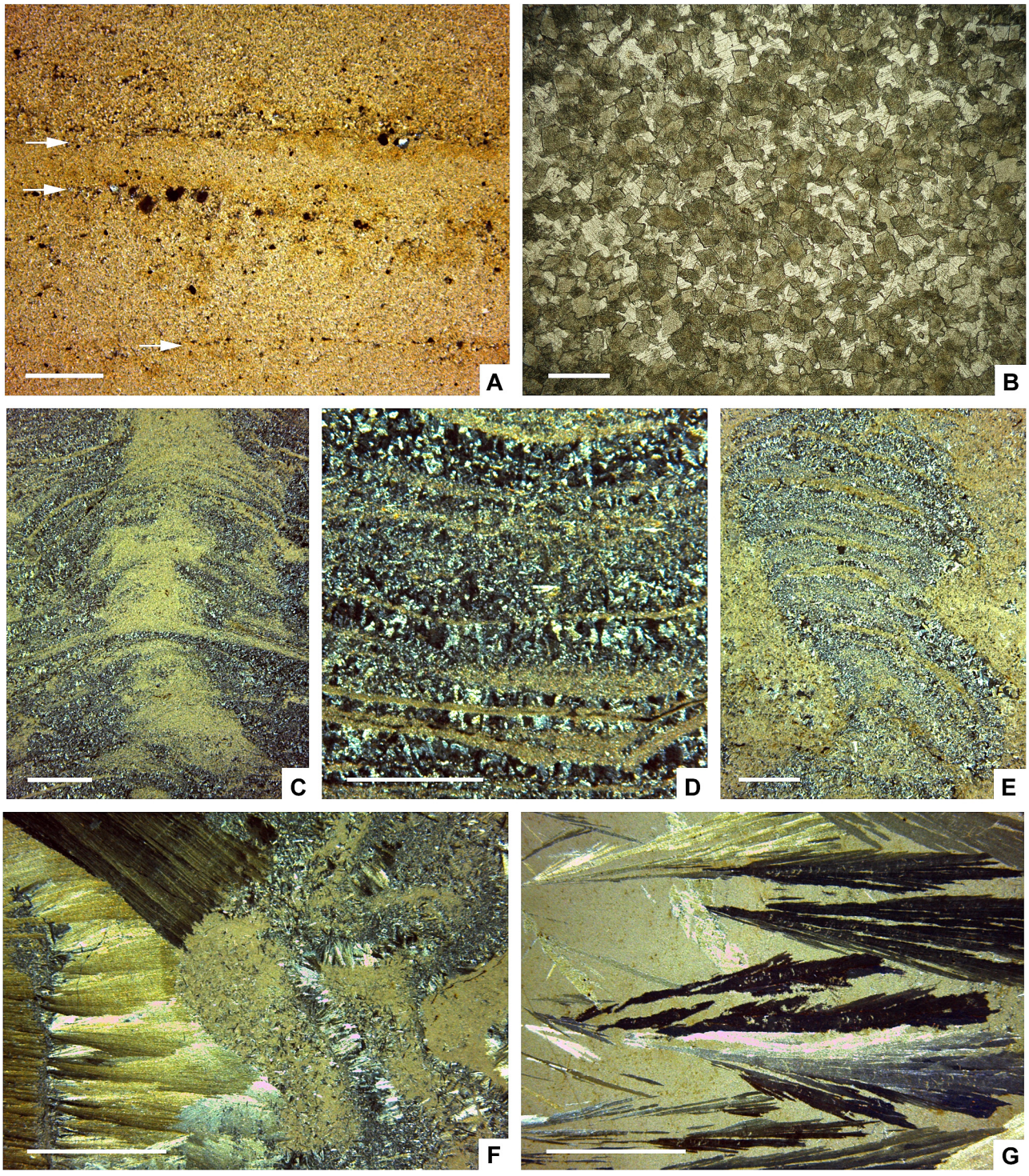

Fig. 5. Thin-section photomicrographs of the Koniakari cap carbonate and Nioro chert in plane-polarised light. A. Well-laminated micrite/microsparite couplets (contacts are arrowed; K1). B. Undolomitized pseudosparite with euhedral to subhedral calcite crystals (K1). C–E. Microbial domal-to-columnar stromatolites alternating microsparite calcite with thin isopachous *palisadic barite cement* (K2). F–G. Upper contact of barite dyke showing development of radiate blade- and acicular barite crystals in a partly dolomitized host rock (K2); scale bars = 2 mm (A, E), 0.6 mm (B), 5 mm (C, F–G) and 1 mm (D).

ba2) and those post-dating the first solution event (*si1*, *si2*, *do2*, *ca2* and *ba3*) are also recognised in the overlying chert.

Three processes were contemporaneous with biofilm and mat growth: calcite precipitation and neomorphism (*ca1*) and partial dolomite replacement (*do1*). Type-1 dolomite (*do1*) comprises up to 20 % of the dolomitized rock volume in section K1 and 60 % in K2, and consistently follows stratiform geometries with diffuse outlines with the original *ca1* phase. Matrix dolomite advanced by selective microsparitic replacement, reflecting the patchy distribution of matrix dolomite. Local fissuring (F1) was occluded with barite (*ba1*), a mineral that also occurs as palisadic interbeds on mats and stromatolites, and as dispersed authigenic crystals crosscutting *ca1* and *do1* (Fig. 5C–G).

A major pH change led to partial dissolution of carbonates (Fig. 7A) and subsequent silicification (also responsible for silicification of argillaceous mud in the overlying chert). Silica (*si1*) occurs as microquartz and chalcedony partly occluding millimetre- to centimetre-scale vugs

	mineral cement	occluded porosity and replacement	shape	size
mat growth	1. Calcite (*ca1*)	micrite to neomorphic microsparite	anhedral	< 5 μm
mat growth	2. Dolomite (*do1*)	microsparite to pseudosparite	subhedral	< 80 μm
	fissuring (F1)			
mat growth	3. Barite (*ba1*)	lining veins and replacing carbonate	acicular and rosette	< 1 mm
	solution			
	4. Silica (*si1*) + Ba-rich silica (*si2*)	occluding vugs + replacement	bladed to blocky	<100 μm
	fissuring (F2)			
	5. Silica (*si3*) + barite (*ba2*) + Fe-rich silica (*si4*)	lining veins and occluding cracks	fibrous, botryoid and drusy	<100 μm
	6. Dolomite (*do2*)	replacement	euhedral (lozenge-shaped)	<100 μm
	fissuring (F3) + solution			
	7. Illite infiltration	partially occluding vugs	honey comb	<30 μm
	8. Calcite (*ca2*) + barite (*ba3*)	dedolomitization and remaining porosity	anhedral	<100 μm

Fig. 6. Summary of diagenetic processes recorded in the cap carbonate and chert of the Kayes area; steps numbered in chronological order.

(Fig. 7A, B). The remaining porosity was occluded with black Ba-rich silica (*si2*; Fig. 7A–D).

Disrupted substrates were affected by two further fissuring and solution processes (F2 and F3 in Fig. 6), which separated silicification from dolomite precipitation. Silica (*si3*) and barite (*ba2*) sealed shrinkage (soft-sediment deformation structures) as isopachous fibrous (*si3f*), isopachous botryoidal clusters of chalcedony (*si3b*) and drusy mosaics (*si3d*), and sheet cracks as palisadic crusts (*si4*) of fibrous and equant silica (Fig. 7E–G). In section K2, the end of silicification is marked by the occurrence of scattered to clustered, euhedral dolomite rhombs (*do2*; Fig. 7C) that grade into prevalent (fabric-destructive), dense interlocking mosaics of anhedral dolomite. After another episode of fissuring (F3) and solution, a new generation of vugs was occluded with illite infiltration (Fig. 7D), calcite (*ca2*, interpreted as dedolomite; Fig. 7C–E) and barite (*ba3*; Fig. 7H). Dedolomite consists of entire rhomb-shaped crystals or, more frequently, thin, rhomb-shaped crystalline rims. They occur following stratiform geometries and are mainly associated with brecciated pockets in K2. The presence of sphalerite and haematite grains scattered throughout the Nioro cherts suggests high-temperature hydrothermal activity in neighbouring seep networks (Fig. 7H). Dolomite mosaics with planar crystal boundaries (idiotopic crystals) characterise precipitation temperatures lower than 50–60 °C (i.e., shallow burial; Warren, 2000).

Similar diagenetic sequences, including fissuring, solution, silicification, dolomitization and dedolomitization of authigenic dolomite rhombs were previously reported in other laterally equivalent cap carbonates of the Adrar of Mauritania and the Walidiala valley of the Senegal/Guinea border (Álvaro et al., 2007; Shields et al., 2007b). The same authors interpreted these processes as a result of episodic tectonic activity during the sedimentation and early diagenetic processes recorded in marine substrates, which recorded contemporaneous input of felsic and mafic clasts, and the influx of hydrothermal processes.

7. Geochemical characterisation

Five targets were selected for geochemical analysis: (i) the carbon/oxygen isotopes of the cap carbonate at section K1, (ii) the carbon/oxygen isotopes of the stromatolites that developed under the contemporaneous influence of Ba-rich discharging fluids at section K2, (iii) the carbon/oxygen isotopes of the diagenetic calcite and dolomite cements, (iv) the S/Sr isotope ratio of the barite occluding synsedimentary fissures and fractures, and needles interlayered in domal stromatolites, and (v) the composition of fluid inclusions in barite crystals.

7.1. Chemostratigraphy of the cap carbonate

Carbon isotope values ($\delta^{13}C_{PDB}$) of bulk microsparitic (calcite, *ca1*) limestone from section K1 (Fig. 2D, Suppl. Table 1) range between −6.8 ‰ and −1.5 ‰ (mean = −4.15; n = 20 over 6.1 m). Oxygen isotopes values ($\delta^{18}O_{PDB}$) range between −11.8 ‰ and −5.0 ‰ (mean = −8.26; n = 20). Although covariance between $\delta^{13}C$ and $\delta^{18}O$ is not significant (r^2 = 0.447; Fig. 2C), suggesting a negligible effect of meteoric alteration, $\delta^{18}O_{PDB}$ values are slightly lighter than other datasets from laterally equivalent cap carbonates of the Taoudeni Basin, which range from −8.6 ‰ to −5.9 ‰ and −5.8 ‰ to −4.5 ‰ in the Adrar of Mauritania (Álvaro et al., 2007; Shields et al., 2007a), from −8.9 ‰ to −3.2 ‰ in the neighbouring Volta Basin (Nédelec et al., 2007), and from −9.6 ‰ to −6.2 ‰ and −9.0 ‰ to −5.4 ‰ in the vicinity of Koniakari and Goumare, Mali (Shields et al., 2007b) (see setting in Fig. 1A). An explanation for the lighter $\delta^{18}O$ values in the Kayes area can be related to the intrusion of Permo–Trias dolerites that cover the study area (Rossi, 1982; Fig. 1B), reflecting post-depositional alteration and diagenetic resetting of samples controlled by thermal overprint. However, the absolute isotopic values were affected in a similar way throughout the entire section, and the profile potentially preserves the original chemostratigraphic tendency.

$\delta^{13}C_{PDB}$ values form an asymmetric profile, reaching minimum values (shift to −6.8 ‰) close to the bottom and recording upsection a pronounced rise to highly enriched values (−1.5 ‰), despite the interbedding of centimetre-thick black shales in the uppermost part of the cap carbonate (Fig. 2). Similar $\delta^{13}C$ values are known from the Adrar of Mauritania (ranging from −3.7 ‰ to +1.3 ‰ in the Jbéliat area, and from −6.8 ‰ to +3.7 ‰ in the Atar cliffs; Álvaro et al., 2007; Shields et al., 2007a), in the Walidiala valley close to the Senegal/Guinea border (ranging from −6.4 ‰ to −2.6 ‰; Shields et al., 2007b), the neighbouring Volta Basin in Ghana (ranging from −6.5 ‰ to −3.3 ‰; Porter et al., 2004; Nédelec et al., 2007), and the Koniakari and Goumare localities of Mali (ranging from −4.3 ‰ to −0.6 ‰ and from −3.9 ‰ to −0.4 ‰, respectively; Shields et al., 2007b). Symmetric shifts, displaying a composite negative to positive trend upsection, in other Marinoan cap carbonates are worldwide recorded in deeper substrates (Halverson et al., 2005; Corsetti et al., 2006). However, only the upper part (positive trend) of these symmetric shifts is recorded throughout the Taoudeni Basin, as a result of their record on relatively shallower substrates. In the latter, as discussed above, the delayed beginning of carbonate production was controlled by onlapping geometries (related to broad transgression) throughout an inherited glaciogenic palaeorelief (Álvaro et al., 2007).

7.2. Carbon and oxygen isotopes of microbial build-ups

Stable-isotope analysis of the stromatolites that cap the barite dykes at section K2 is notably heterogeneous. $\delta^{13}C_{PDB}$ values range from −43.2 ‰ to −4.8 ‰ and $\delta^{18}O_{PDB}$ values from −9.8 ‰ to −13.2 ‰ (Fig. 8; Suppl. Table 1). The lowermost $\delta^{13}C$ values (<−30 ‰) were obtained from the microsparite/barite couplets that form the domal stromatolites. By

contrast, the $\delta^{18}O$ values, which are relatively homogeneous and quite negative, seem to be mainly controlled by elevated temperatures during sedimentation or burial diagenesis. $\delta^{13}C$ variability resulted from mixing of different carbon sources. The lowest $\delta^{13}C$ ratios are characteristic for seep carbonates, and such values are widely accepted as criteria for methane-derived carbonate (Han et al., 2004; Wang et al., 2008). However, other values close to barite-free carbonates of section K1 do not suggest interaction with ^{13}C-depleted methane, which may be interpreted as due to a different carbon source (e.g., CO_2 gas hydrates) or simply a result of photosynthetic activity (DiFilippo et al., 2003).

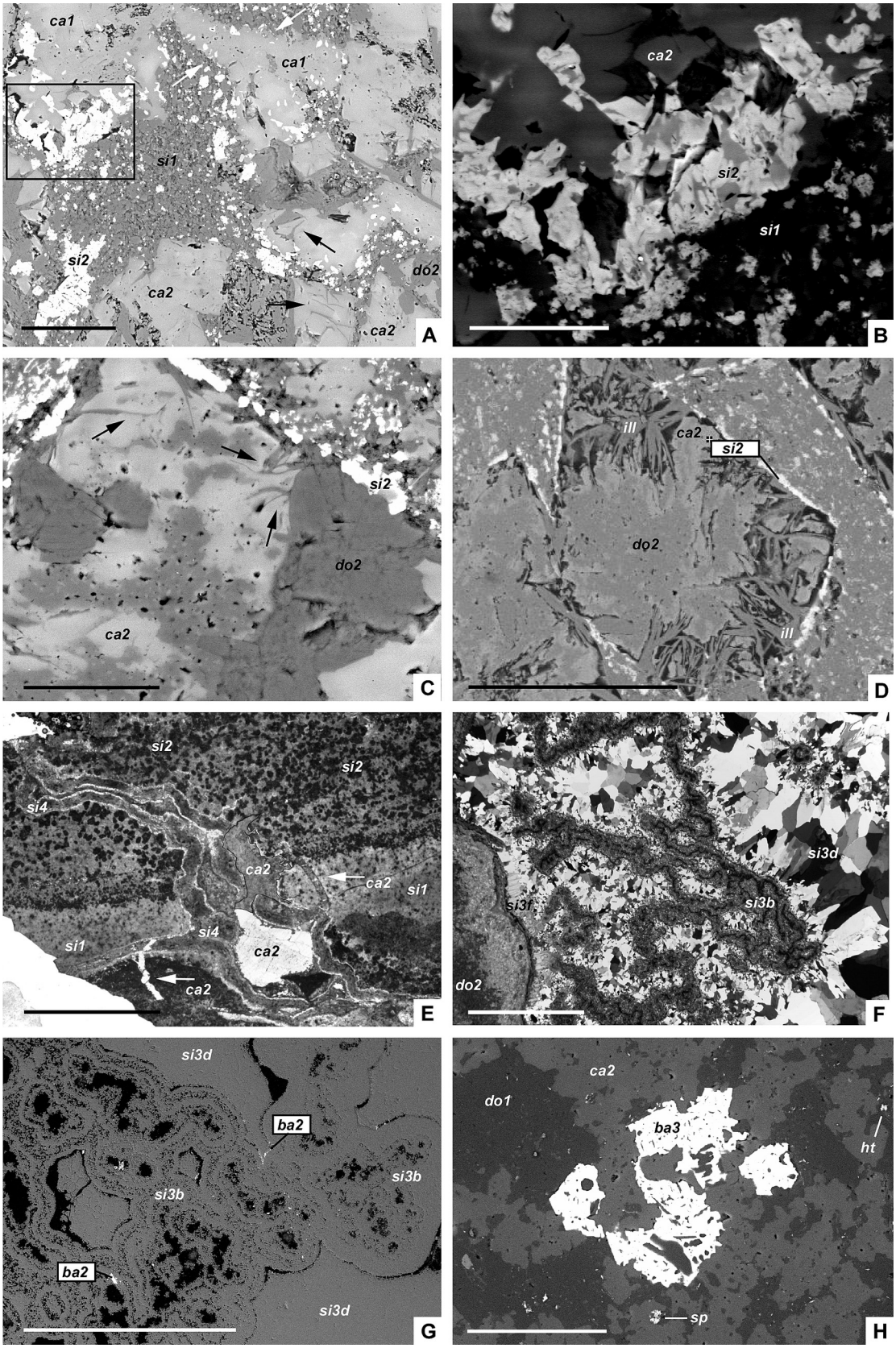

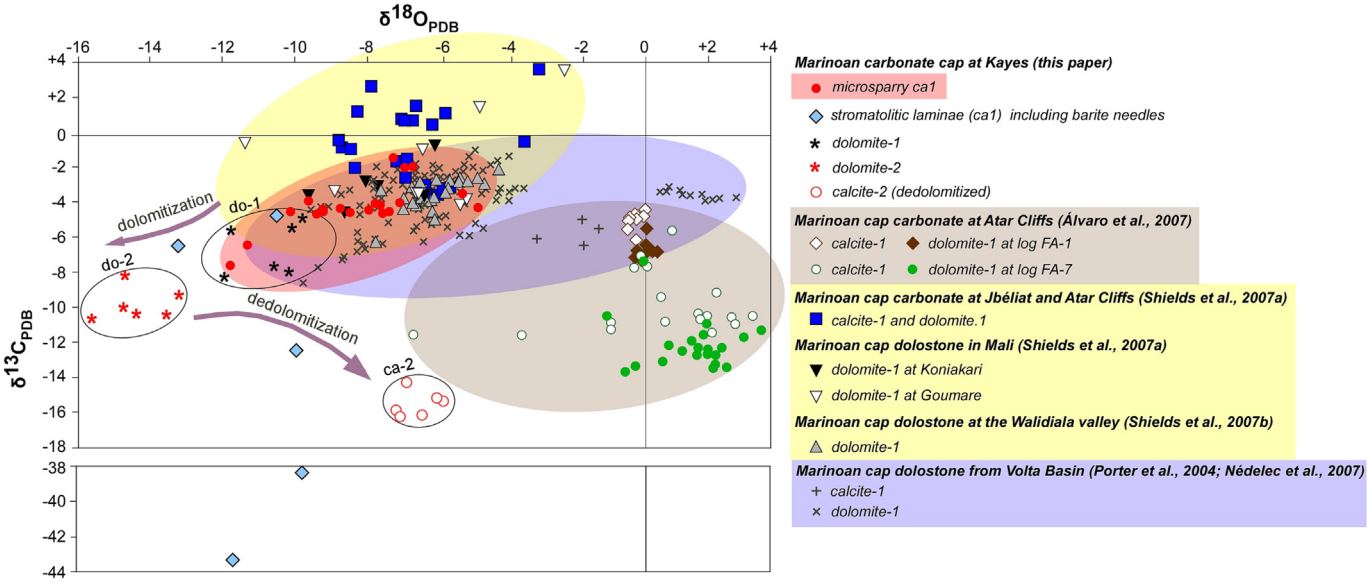

Fig. 8. Stable carbon and oxygen isotope dataset plot for the different calcite and dolomite, primary and diagenetic phases recorded in the cap carbonate of Kayes, compared to coeval cap carbonates from the Adrar sub-basin and the Volta Basin in the West African craton (Álvaro et al., 2007; Shields et al., 2007a, 2007b; Porter et al., 2004; Nédelec et al., 2007).

7.3. Carbon and oxygen isotopes of diagenetic carbonate

The diagenetic calcite and dolomite phases recorded in the cap carbonate display different carbon and oxygen isotopic values. The $\delta^{13}C_{carb}$ and $\delta^{18}O_{carb}$ values of the first dolomitization phase (partial replacement by *do1*) range from −6.8 to −2.0 ‰ and from −11.8 to −5 ‰, respectively (Suppl. Table 1). In contrast, the subsequent dolomitization phase (mosaics of euhedral rhombs *do2*) shows narrower ranges of $\delta^{13}C_{carb}$ (from −8.3 to −4.9 ‰) and $\delta^{18}O_{carb}$ (from −11.9 to −9.8 ‰) values. Finally, the sampled entire rhomb-shaped calcite crystals, representing a final dedolomitization phase (*ca2*), display the narrowest ranges of $\delta^{13}C_{carb}$ (from −16.2 to −14.2 ‰) and $\delta^{18}O_{carb}$ (from −7.3 to −6 ‰) values.

A distinct trend is shown (Fig. 8) from the original preserved microsparry calcite (*ca1*) to the successive dolomite cements (*do1*, *do2*) becoming progressively lowered in both $\delta^{13}C$ and $\delta^{18}O$ values. Cement ratios are distinct, suggesting that they precipitated from different fluids at different temperatures. This fits well with the inferred early diagenetic origin of dolomite and would reflect the interaction of both meteoric waters and progressively elevated temperatures of precipitation, linked to lower $\delta^{18}O$ values (Warren, 2000). In contrast, the final calcite mosaics induced by dedolomitization (*ca2*) reflect a different trend to higher values of $\delta^{13}C$ and lower values of $\delta^{18}O$. Fluid-driven dedolomitization required the influence of fluids with low Mg^{2+}/Ca^{2+} ratios, able to remove the liberated Mg^{2+} to keep dolomite undersaturation (Ayora et al., 1998). Sources of ^{13}C-depleted dissolved inorganic carbon (DIC) could be related to both oxidation of CH_4 (e.g., involving the anaerobic oxidation of methane) and the decomposition of organic material by thermal and/or microbial oxidation.

7.4. Strontium and sulphur isotopes of barite crystals

Barite crystals sampled as infills of synsedimentary fractures in section K2, sealed by chemoherms, have yielded strontium isotope ratios ($^{87}Sr/^{86}Sr$) ranging over a narrow range of 0.70820–0.71194. These are lower than those yielded by the cap carbonate from the neighbouring section K1 (0.71226–0.71491; Suppl. Table 1), about 10 km away from the venting of Ba-rich fluids. The latter represents somewhat anomalous data by comparison with those reported from other basins, across the Cryogenian–Ediacaran transition, which point to an increase in the $^{87}Sr/^{86}Sr$ ratio from 0.7066 to 0.7082 (e.g., in the Bitter Springs Formation of Australia, the Hayhook Formation of the Mackenzie Mountains in Canada, and the Maiberg Formation in Namibia; Walter et al., 2000; Halverson et al., 2005, 2007). This sharp increase in the aftermath of the Marinoan glaciation has been interpreted as a consequence of high silicate weathering rates from elevated pCO_2 and/or long-lived ocean stratification, leading to a surface ocean strongly influenced by radiogenic runoff from the continents (Hurtgen et al., 2006; Halverson et al., 2007; Shields, 2007). The higher Sr isotope values reported in the cap carbonate of Kayes may reflect shallower conditions of a peritidal-dominated substrate than other reported basins, as well as the active erosion of palaeoreliefs associated with the coeval input of acidic explosive volcanism in the Taoudeni Basin (Álvaro et al., 2007; Shields et al., 2007a).

Because of the presence of carbonate, chert and other contaminant minerals encased in the barite samples, several leaching techniques were applied by Shields et al. (2007a) to obtain the Sr isotope composition of barite samples. Selected samples were leached with ammonium acetate, HBr, HCl and HNO_3, which resulted in significantly different

Fig. 7. Diagenetic features recorded in the Koniakari cap carbonate and Nioro chert at K2. A. Partly silicified uppermost part of cap carbonate with embayed (via dissolution) contacts of primary calcite (*ca1*) relics (white arrows) and secondary porosity occluded with silica (*si1* and *si2*), authigenic dolomite (*do2*) and dedolomite (*ca2*); black arrows mark tensional fissures preserved in partly dedolomitized rhombs. B. Detail of boxed area with distinction of poor silica (*si1*) and barite-rich silica (*si2*), the latter showing different degrees of impurity. C. Detail of partly dedolomitized rhomb outlined by barite-rich silica; black arrows mark tensional fissures unaffected by dedolomitization. D. Partly dedolomitized rhomb with secondary porosity occluded with illite (*ill*). E. Crosscutting relationships of cracks occluded with silica (*si4*, first generation) and calcite (*ca2*, second generation) in a host rock silicified with pure (*si1*) and barite-rich silica (*si2*). F. Multiple generations of silica cements: isopachous microquartz (*si3f*), botryoid chalcedony (*si3b*) and drusy megaquartz (*si3d*) occluding dolomite-hosted (*do2*) shrinkage cracks. G. BSE aspect of shrinkage-like infill with identification of a phase of barite precipitation (*ba2*) separating the botryoid and drusy phases. H. Textural aspect of anhedral calcite (*ca2*) affecting a dolomite (*do1*) that alternates with shale in the chert unit; remarks the last precipitation phase of barite (*ba3*) and the presence of scattered crystals of haematite (*ht*) and sphalerite (*sp*). SEM-BSE photomicrographs (A–D and G–H) and photomicrographs in plane-polarised light (E) and crossed nicols (F). Abbreviations taken from the text; scale bars = 100 μm (A), 50 μm (B, H), 30 μm (C–D), 5 mm (E), 2 mm (F), and 1 mm (G).

values. Therefore, differential leaching of contaminant phases necessarily affected the results. Only the lowest values for $^{87}Sr/^{86}Sr$ (0.7077–8) yielded by the different leaches were selected as consistent, concluding that the mineralising fluid was mainly derived from the ocean (Halverson et al., 2007). In our study, barite samples were leached with HCl, HF and HNO_3, and the ratios reached higher values ranging between 0.7082 and 0.7119. The lowest values of our analysis match well with the lowest values of Shields et al. (2007a), but other factors than differential leaching should be considered.

Marinoan cap carbonates in Brazil offer sharp differences in $^{87}Sr/^{86}Sr$ ratios that have been interpreted differently. The Sete Lagoas cap carbonate (Bambuí Group) displays a positive excursion ($^{87}Sr/^{86}Sr$ ratio rising from 0.7074 to 0.7082) locally affected by episodic subaerial exposure, which triggered meteoric modification and shifting of $^{87}Sr/^{86}Sr$ ratios towards higher values (>0.710) and $\delta^{18}O$ towards lower values (Paula-Santos et al., 2017; Caxito et al., 2018). Uppermost Ediacaran strata from the Bambuí Group show extremely low $^{87}Sr/^{86}Sr$ ratios, around 0.7075, which were interpreted as a result of restricted scenarios disconnected from open marine water, where the lack of homogenisation would have induced anomalously low ratios (Paula-Santos et al., 2017). In contrast, the Araras Group presents more stable $^{87}Sr/^{86}Sr$ values, ranging between 0.7075 and 0.7079 in the lower formations and reaching 0.7087 in the upper columnar-stromatolite-bearing limestone lenses (Alvarenga et al., 2008).

Sulphur isotope values of the Kayes barite ($\delta^{34}S_{CDT}$) range from 29.9 to 34.3 ‰, which are broadly similar to values from the Salitre Formation at Nova Redenção (33.6 to 41.0 ‰; Misi et al., 2005), and the Sete Lagoas Formation in the Montalvânia region (48.2 to 50 ‰; Gomes, 2005), Brazil. In contrast, they are somewhat heavier than those reported in the same Sete Lagoas cap carbonate and in the Januária area (25.7 to 32.2 ‰; Okubo et al., 2020) and the Salitre cap carbonate in the Irecê Basin (25.2 to 32.8 ‰; Kyle and Misi, 1997) in Brazil. Remarkably, the isotopic values of other barite precipitations encased in Marinoan cap carbonates display broader ranges, such as those reported from the Jbéliat of Mauritania (20.3 to 45.6 ‰; Shields et al., 2007a) and Songlin in South China (21.7 to 45.5 ‰; Peng et al., 2011). In addition, the Cryogenian–Ediacaran transition also recorded a $\delta^{34}S$ rise in sulphates ranging from 18 to 28 ‰, and reaching peaks close to 34 ‰ close to the base of the Cambrian (Walter et al., 2000; Hurtgen et al., 2004, 2005; Shields et al., 2004). Our data also fit well with similar values yielded in the aftermath of the Marinoan glaciation in Namibia (Hurtgen et al., 2002, 2006), which display highly variable ranges illustrating a lateral $\delta^{34}S$ gradient from restricted to open-shelf settings. Variations can be interpreted as the result of regional variation in the $\delta^{34}S$ of marine sulphate, different origins for barite in different units, or diagenetic alteration (Okubo et al., 2020) or the re-introduction of sulphate into the basin from incursions of meteoric groundwaters in peritidal and shallow-water substrates, as the Kayes case-study. $\delta^{34}S_{sulfide}$ data are not available for comparison because of the rare preservation of pyrite in these substrates.

Sulphur isotopic compositions of the barite samples at Jbéliat and Mali (Shields et al., 2007a) show broad ranges between 20 and 46 ‰. These values support a marine source for the sulphate in the barite. The range would suggest considerable sulphur isotope fractionation from the primary seawater source. According to Torres et al.'s (2003) analysis of present-day sedimentary barite, the lowermost $\delta^{34}S$ values should likely point to seawater values, because sulphate reduction naturally tends to enrich the sulphate reservoir in ^{34}S (e.g., Jewell, 2000; Clark et al., 2004; Shields et al., 2007a).

We used Paytan et al.'s (2002) test, based on S/Sr isotopes, to check the environmental interpretation documented above: if Ba-rich fluids were expelled into seawater from fractured seeps, the combined S and Sr isotope ratios of the diagenetic barite would be distinctive. As illustrated in Fig. 9, the S isotope ratios of the Kayes barite crystals were slightly greater than contemporaneous seawater, probably due to sulphate reduction occurring when fluids were expelled into the substrate, depleting the pore-water sulphate in the light S isotope and, as a result, ensuing barite crystals with S isotope ratios slightly greater than those of seawater.

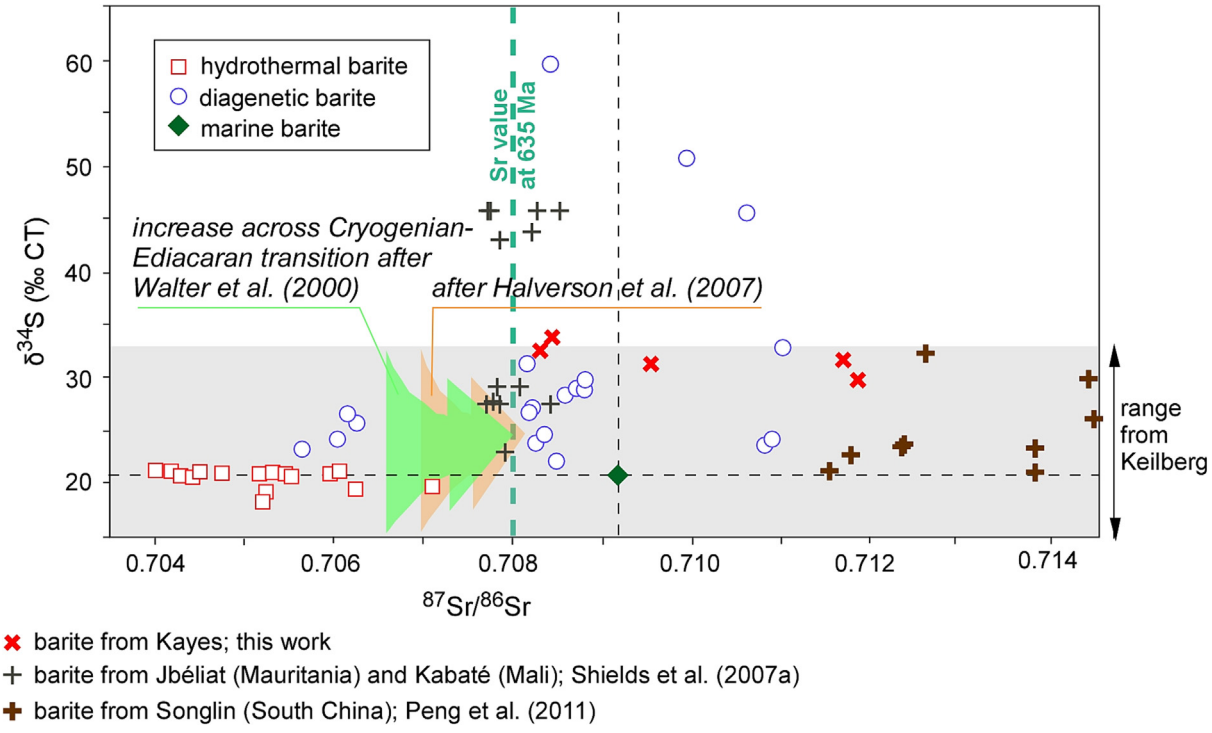

Fig. 9. Plot of strontium and sulphur isotopes for barite samples from different present-day depositional environments (modified from Paytan et al., 2002), with indication of values from Kayes, $\delta^{34}S$ ranges documented in the lowermost Ediacaran Keilberg Member from Namibia (Hurtgen et al., 2006), and the $^{87}Sr/^{86}Sr$ increase reported across the Cryogenian–Ediacaran transition by Walter et al. (2000) and Halverson et al. (2007).

The strontium and sulphur isotopes of barite support mixing of barium- and methane-rich fluids, derived from groundwater seepage, with oxygenated sulphate-rich seawater during rapid marine transgression (Shields et al., 2007a). Further comparison of Ba isotopic data with modern datasets yielded by barite precipitating in terrestrial, pelagic, hydrothermal and cold seep environments (Crockford et al., 2019) would constrain better the genesis of Ba in the cap carbonate of the Kaarta Mountains.

7.5. Fluid inclusions in barite crystals

Barite occurs as a wide range of crystal habits, including acicular/radiating, bladed and tabular crystals. Crystals with different habits commonly concur in different sectors of a single sample. Their size ranges from <0.1 μm up to 10 mm. Linkan microthermometry analyses were only made on inclusions ranging from 5 to 8 μm in size. Fluid inclusions (FIs) were investigated in barite-occluding fissures and stromatolite-bearing primary pores (Suppl. Table 2). They contain primary fluid inclusion assemblages or FIAs (i.e., scattered inclusions and small clusters and trails following growth zones) that show variable sizes and irregular outlines. At room temperature, they are mostly all-liquid but the largest inclusions show two-phase (liquid + vapour) FI with liquid percentages about 90–95 %. FI freezes at temperatures between −54 to −42 °C, usually around −47.8 °C (T_n, $n = 20$). Upon reheating, the final melting of ice (T_{mice}) ranges from −8.9 to −5.4 °C. FI homogenisation (T_h) occurs to the liquid usually from 174 to 222 °C. No correlation was found between the sizes of fluid inclusions and T_h values. Considering a H_2O–NaCl system, salinities would reflect 11–19.7 NaCl wt% equivalents (Davis et al., 1990; Bodnar and Vityk, 1994; Goldstein and Reynolds, 1994). Plotting salinity vs. T_h (Kesler, 2005), the dataset of fluid inclusions falls into the fields of basinal and seawater fluids, which suggest the interplay of two mineralizing fluids (Suppl. Fig. 1).

Laser Raman analyses were accompanied independently to calculate the composition of fluid inclusions in smaller barite crystals, <2 μm in size. The Raman spectra for methane hydrate split into two peaks, one of them represented with a prominent peak at 2914 (±1) cm^{-1} (Uchida et al., 2000; Chazallon et al., 2007; Choukroun et al., 2007; Hester et al., 2007; Lin et al., 2007). This peak was identified in the barite crystals of K-2 section (Fig. 10) supporting the presence of methane; the remaining Raman peaks are related to the barite host crystal.

8. Biomarkers from the cap carbonate

Although the majority of worked up samples were rather lean in organics, samples from level K1–28 (Fig. 11) show the typically observed molecular distribution and were characterised by nearly identical results obtained from sample interiors and sample exteriors, supporting the syngenetic features of the observed signatures. Alkanes (peaking around nC_{16-18}) and acyclic isoprenoids (Pr < Ph) show an inconspicuous pattern and point towards deposition under non-oxidising conditions (Ten Haven et al., 1987, 1988). Amongst pentacyclic triterpenoids, a near-absence of C_{28} bisnorhopanes is accompanied by C_{29}/C_{30} hopane ratios of 2.23, a signature that tends to be more abundant in organic matter preserved in carbonate (e.g., Seifert and Moldowan, 1986; Waples and Machihara, 1991). Under strongly reducing conditions, biosynthesized C_{35} hopanepolyols tend to be preferentially reduced (rather than oxidised and

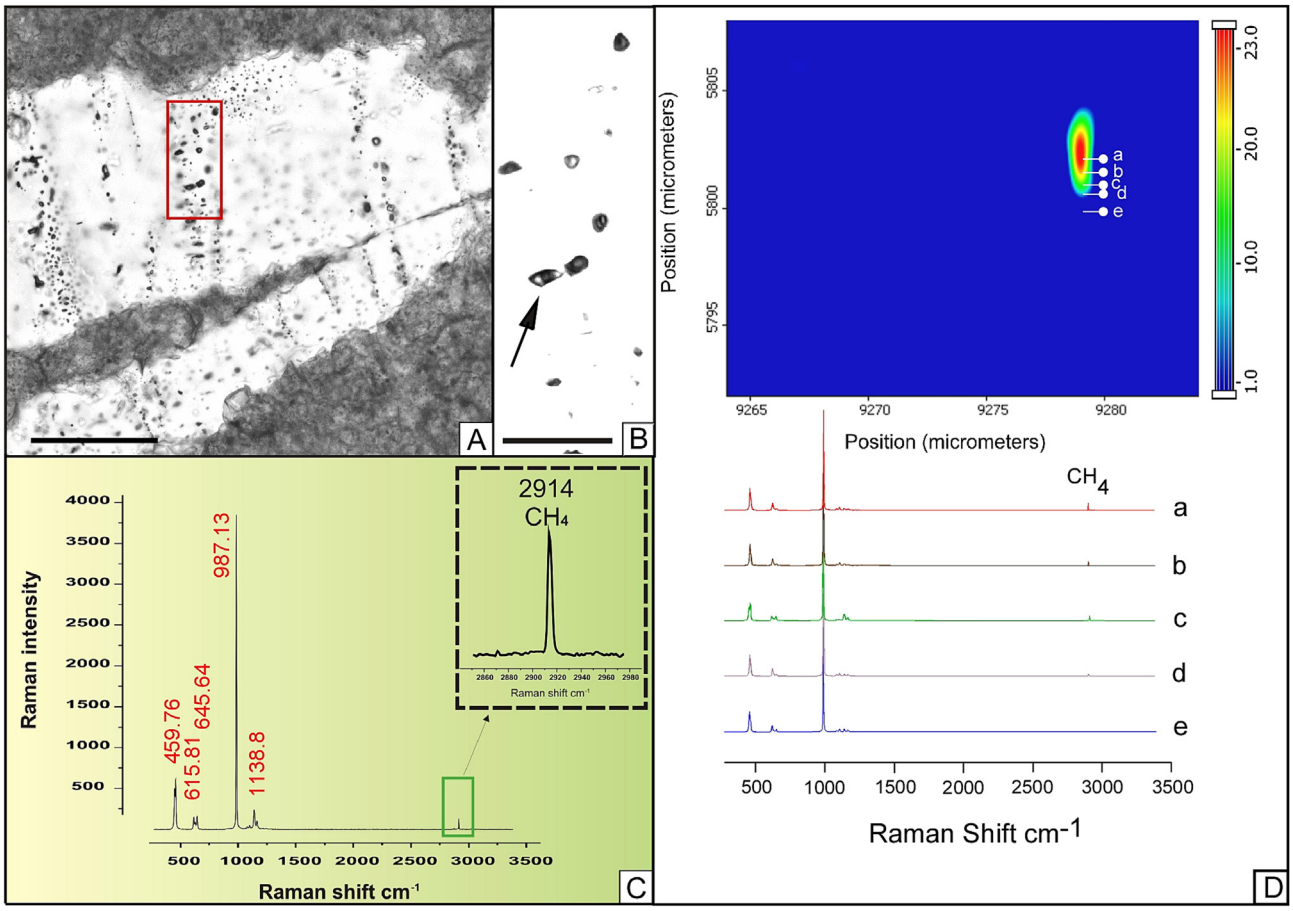

Fig. 10. A. Photomicrograph showing the distribution of CH_4 inclusions in barite mainly parallel to cleavage planes. B. Detail of previous boxed area illustrating analysed bubble-bearing fluid inclusion. C. Raman spectra of arrowed fluid inclusion at room temperature; see peak position of CH_4 at 2914 cm^{-1} and peaks in red of barite host-mineral; scales (A) = 65 μm and (B) = 10 μm. D. Mapping mode of the Raman signal evolution constraining an inclusion about 1 × 4 μm in size and spectra at different inclusion depths (see *a* to *e* levels).

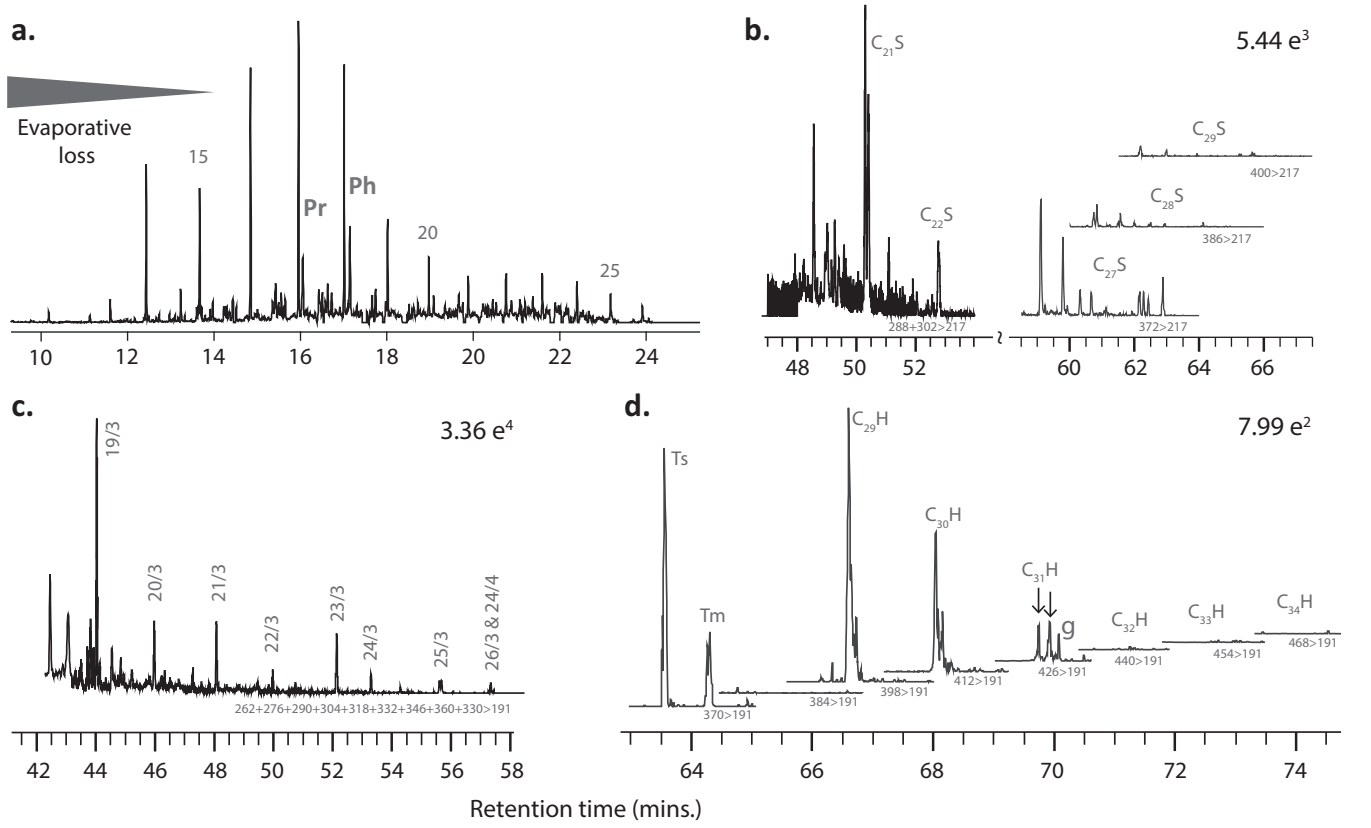

Fig. 11. Characteristic molecular composition of hydrocarbons from the cap carbonate of the Koniakari Group (sample K1–28, interior). Chromatograms obtained by GC-TOF-MS (a) and GC-QqQ-MS (b–d) showing (a) the distribution of *n*-alkanes and linear isoprenoids pristane and phytane on *m/z* 85 (*m/z* 149 was subtracted to remove laboratory-introduced and interfering plasticiser peaks that were present in samples and blanks), and the distribution and relative abundance of (b) steranes (S), (c) tri- and tetracyclic terpenoids, and (c) hopanes (H). Mass transitions used in GC–MS/MS are shown below chromatogram traces; signal intensities are shown on the top right above each chromatogram. Note the high relative abundance of truncated steranes and the dominance of C_{27} steranes amongst C_{27}–C_{29} species. Pr: pristane; Ph: phytane; Ts: 18α(H)22,29,30 trisnorneohopane; Tm: 17α(H)22,29,30 trisnorhopane; ɣ, gammacerane.

decarboxylated), giving rise to high relative abundances of extended homohopanes (Peters and Moldowan, 1993), which is not observed in the analysed samples. Under less reducing conditions, the principal end products predominantly consist of C_{29}–C_{31} hopanes, whose relative abundance was suggested to be affected by the degree of initial functionalization-hexafunctionalized hopanoids giving rise predominantly to C_{29} (30-nor)hopanes (Bobrovskiy et al., 2018 and references therein). A predominance of such 30-norhopanes may potentially point towards a relevant contribution of methanotrophs, since hopanoids with hexafunctionalized side-chains appear to be prevalent in Type I methanotrophic bacteria (Neunlist and Rohmer, 1985; Zundel and Rohmer, 1985; Brocks and Summons, 2003). A-ring methylated hopanes (2α- and 3β-methylhopanes) were not observed. Hopane abundances were too low to confirm a methanotrophic source via compound-specific ^{13}C investigation (e.g., Luo et al., 2019) and it should be noted that enhanced thermal maturation can also lead to a lowering of the homohopane index and an increase in values for the C_{29}/C_{30} hopane parameter (Peters and Moldowan, 1993). Nevertheless, a relevant role of methanotrophic bacteria in the Koniakari depositional environment could potentially be supported by the presence of gammacerane. Likely derived from tetrahymanol, gammacerane is typically considered characteristic for stratified conditions in the water column, where its precursor lipid is produced by bacterivorous ciliates in the absence of a significant algal ecosystem component, since ciliates do not biosynthesize tetrahymanol when acquiring sterols through their diet (Sinninghe Damsté et al., 1995). Recently however it was shown that some bacteria carry the biosynthetic capacity for tetrahymanol production, including gammaproteobacterial Type I methanotrophs (Banta et al., 2015). In the presence of preserved steranes, a bacterial source of tetrahymanol cannot be excluded. With tricyclic terpenoid values of 0.32 for the C_{22}/C_{21} and 0.36 for the C_{24}/C_{23} parameters, the biomarkers plot outside the fields that are characteristic for the majority of Phanerozoic oils and rocks (e.g., Al-Ameri et al., 2009), but would indicate a peritidal to marine shale depositional facies from the perspective of solely the C_{22}/C_{21} parameter, whereas indicating marine carbonate facies if only considering the C_{24}/C_{23} parameter. In contrast to the elevated C_{29}/C_{30} hopane signature, considered characteristic for carbonate facies, all observed sterane series (C_{27}–C_{29}) are characterised by elevated abundances of diasteranes (dia/regular = 2.37 for cholestanes), which was traditionally considered a hallmark of shale-dominated lithologies given that the steroidal rearrangement is thought to be clay catalysed (Rubinstein et al., 1975; Sieskind et al., 1979). Counterintuitive high abundances of diasteranes in carbonate-hosted organic matter can however be reconciled by the later finding that the molecular conversion to diasteranes appears to be controlled by clay/TOC ratios (Van Kaam-Peters et al., 1998a, 1998b), and by the fact that values of the dia-/regular sterane parameter can increase during progressive thermal maturation (Peters and Moldowan, 1993). Both explanations may apply to the Koniakari cap carbonate, which is characterised by overall low TOC values and a mildly elevated thermal maturity, as shown e.g., by Ts/(Ts + Tm) values of 0.63. In terms of the relative abundance of C_{27}, C_{28} and C_{29} steranes, the here reported rocks fall into a small group of earliest Ediacaran deposits that reflect the transition between pre–Cryogenian ecosystems, whose molecular assemblages completely lack any traces of C_{29} 24-ethylsteranes, and the typical C_{29}-dominant steroidal signature that characterises the vast majority of globally deposited Ediacaran sediments (Hoshino et al., 2017). The complete absence of fossil steranes $>C_{28}$ in strata antedating the Cryogenian was attributed to the progressive evolution of the steroid biosynthetic

pathway, as previously suggested by Bloch (1994), where the emergence of the second sterol-C_{24}-methyltransferase sets apart C_{27} and C_{28} vs. C_{27}–C_{29} steroidal products. The global transition of cholestanoid (C_{27}) to stigmastanoid (C_{29}) algal ecosystems across the Snowball Earth events, possibly reflecting a transition of red to green algae, was initially considered to have occurred contemporaneously to the rise of algae to ecological dominance (Brocks et al., 2017). A brief post–Cryogenian continuation in the complete absence of C_{29} steranes, as seen in the Araras Group (van Maldegem et al., 2019), and the here reported dominance of C_{27} steranes ($C_{27}/C_{29} = 6.36$) in parallel with overall steroidal abundances exceeding those of bacterial hopanoids (sterane/hopane = 3.26), suggest a more complicated transition, where the change of cyanobacterial to algal primary producers may have preceded a global shift in the relevance of red- to green-algal lineages. The microbial contribution to carbonate production, detected by their biogenic textures, may have been enhanced by anaerobic oxidation of methane, which was transported from deeper venting fluids. Seepage of methane-bearing fluids may have been controlled by the remobilisation and alteration of hydrocarbons encased in the underlying Mesoproterozoic Atar, Irma and Dimamou groups (Deynoux et al., 2006; Álvaro and Vizcaïno, 2012).

9. Conclusions

In the Kaarta Mountains of the Taoudeni Basin, the lithological "triad" (glaciogenic diamictite-cap carbonate-chert) that marks the Cryogenian–Ediacaran transition shows sharp modifications in facies associations over short distances (<10 km). The cap carbonate of the Koniakari Group is representative of both quiescent and disrupted substrates. The former displays a $\delta^{13}C_{PDB}$ profile, attaining minimum values (−6.8 ‰) close to the base and reaching a maximum (−1.5 ‰) at the top. The positive and asymmetric, chemostratigraphic profile reflects relatively shallow substrates, where carbonate productivity was delayed as a result of onlapping patterns on an inherited glaciogenic palaeorelief.

Disrupted substrates are related to the onset of decametre-scale Ba–CH_4 seep networks. Polyphase veining and precipitation of barite as palisadic crystal-filling dykes led to contemporaneous precipitation of stromatolitic chemoherms with interlaminae rich in barite needles. Detailed petrographic and geochemical analyses reveal barite-rich/free couplets of the stromatolitic patches that display $\delta^{13}C$ values ranging from −43.2 ‰ to −4.8 ‰ PDB, indicative of a combination of microbial mediation, probably as alternations of methane, caused by destabilisation of methane hydrates in the subsurface, and photosyntetizer carbon sources. The presence of methane as fluid inclusions in barite crystals was confirmed with Raman. T_h of fluid inclusions (ranging from 174 to 222 °C) provides minimum entrapment temperatures for barite precipitation. Coupled S/Sr isotope analysis in barite crystals allows distinction of diagenetic barite, due to sulphate reduction made when fluids were expelled into the substrate and resulting in barite with S isotope ratios slightly greater than contemporaneous seawater.

Development of fractures and fissures provided a first-order control on fluid migration and setting of build-ups (chemoherms) throughout the Taoudeni Basin. Barite precipitated both below the sediment-water interface and at the seafloor from low-temperature fluids that circulated along fissure networks. The onset of repeated brecciation and fissuring, and multiple episodes of silica, dolomite and calcite (dedolomite) cementation, suggest repeated episodes of fluid flow and subsequent substrate disruption.

Although early diagenetic barite is commonly related to tepee and associated breccias, occurring as void-filling isopachous crustose cements within breccias, such as in the Yangtze Platform of South China, the Dzabkhan Platform of Mongolia and the Adrar of Mauritania, infilling of synsedimentary fracture networks is also relatively common. Pseudo-tepee formation, brecciation and veining have been interpreted as a result of both submarine methane venting and evaporative pumping due to subaerial (supratidal) exposure in substrates of marine-meteoric groundwater mixing. When Ba-rich fluids from seeps are expelled into seawater, fractures are occluded by diagenetic barite in the form of flat, tabular-shaped crystals commonly arranged forming rosettes.

Despite the peritidal character of the Marinoan cap carbonate reported in the Kayes area, the identification of C_{29}-dominant steroidal biomarker signatures, characteristic of stigmastanoid algal blooms, and its interbedding with kerogeneous black shales would point to non-oxidising interrupting conditions.

Data availability

No data was used for the research described in the article.

Declaration of competing interest

The authors declare that they have no known competing financial interests or personal relationships that could have appeared to influence the work reported in this paper.

Acknowledgements

This paper is dedicated to the memory of Ignacio Subías (Zaragoza), who left us when preparing a first draft. The authors appreciate the constructive and thorough reviews by Brian Pratt (Saskatchewan) and an anonymous reviewer. JJA warmly thanks Yaye Bokhoum (Bamako), Jorge Esteve (Madrid) and Daniel Vizcaïno (Carcassonne) for field support. This paper is a contribution to Spanish project PID2021-125585NB-I00 from Ministerio de Ciencia e Innovación.

Appendix A. Supplementary data

Supplementary data to this article can be found online at https://doi.org/10.1016/j.sedgeo.2023.106481.

References

Aharon, P., 1994. Geology and biology of modern and ancient submarine hydrocarbon seeps and vents: an introduction. Geo-Marine Letters 14, 69–73.
Al-Ameri, T.K., Al-Khafaji, A.J., Zumberge, J., 2009. Petroleum system analysis of the Mishrif reservoir in the Ratawi, Zubair, North and South Rumaila oil fields, southern Iraq. GeoArabia 14, 91–108.
Alvarenga, C.J.S., Dardenne, M.A., Santos, R.V., Brod, E.R., Gioia, M.C.L., Sial, A.N., Dantas, E.L., Ferreira, V.P., 2008. Isotope stratigraphy of Neoproterozoic cap carbonates in the Araras Group, Brazil. Gondwana Research 13, 469–479.
Álvaro, J.J., Vizcaïno, D., 2012. Proterozoic microbial reef complexes and associated hydrothermal mineralizations in the Banfora Cliffs, Burkina Faso. Sedimentary Geology 263–264, 144–156.
Álvaro, J.J., Macouin, M., Bauluz, B., Clausen, S., Ader, M., 2007. The Ediacaran sedimentary architecture and carbonate productivity in the Atar cliffs, Adrar, Mauritania: palaeoenvironments, chemostratigraphy and diagenesis. Precambrian Research 153, 236–261.
Ayora, C., Taberner, C., Saaltink, M.W., Carrera, J., 1998. The genesis of dedolomites: a discussion based on reactive transport modeling. Journal of Hydrology 209, 346–365.
Banta, A.B., Wei, J.H., Welander, P.V., 2015. A distinct pathway for tetrahymanol synthesis in bacteria. Proceedings of the National Academy of Sciences USA 112, 13478–13483.
Beeskow, B., Rankin, A.H., Murphy, P.J., Treolar, P.J., 2005. Mixed CH_4–CO_2 fluid inclusions in quartz from the South Wales Coalfield as suitable natural calibration standards for microthermometry and Raman spectroscopy. Chemical Geology 223, 3–15.
Bense, C., 1964. Les Formations Sédimentaires de la *Mauritanie* Méridionale et du Mali Nord-occidental (*Afrique* de l'Ouest). (PhD) Nancy University.
Bertrand-Sarfati, J., Moussine-Pouchkine, A., 1983. Platform-to-basin facies evolution: the carbonates of Late Proterozoic (Vendian) Gourma (West Africa). Journal of Sedimentary Petrology 53, 275–293.
Bloch, K., 1994. Blondes in Venetian Paintings, the Nine-banded Armadillo, and Other Essays in Biochemistry. Yale University Press, Yale.
Bobrovskiy, I., Hope, J.M., Krasnova, A., Ivantsov, A., Brocks, J., 2018. Molecular fossils from organically preserved Ediacara biota reveal cyanobacterial origin for *Beltanelliformis*. Nature Ecology & Evolution 2, 437–440.

Bodnar, R.J., Vityk, M.O., 1994. Interpretation of microthermometric data for H_2O–NaCl fluid inclusions. In: De Vibo, B., Frezzotti, M.L. (Eds.), Fluid Inclusions in Minerals – Methods and Applications. Virginia Tech, Blaksburg, pp. 117–130.

Brocks, J.J., Summons, R.E., 2003. Sedimentary hydrocarbons, biomarkers for early life. In: Schlesinger, W.H. (Ed.), Biogeochemistry. Treatise on Geochemistry 8. Elsevier, Amsterdam, pp. 63–115.

Brocks, J.J., Jarrett, A.J.M., Sirantoine, E., Hallmann, C., Hoshino, Y., Tharika, L., 2017. The rise of algae in Cryogenian oceans and the emergence of animals. Nature 548, 578–581.

Campbell, K.A., 2006. Hydrocarbon seep and hydrothermal vent paleoenvironments and paleontology: past developments and future research directions. Palaeogeography, Palaeoclimatology, Palaeoecology 232, 362–407.

Caxito, F.A., Frei, R., Uhlein, G.J., Dias, T.G., Árting, T.B., Uhlein, A., 2018. Multiproxy geochemical and isotope stratigraphy records of a Neoproterozoic Oxygenation Event in the Ediacaran Sete Lagoas cap carbonate, Bambuí Group, Brazil. Chemical Geology 481, 119–132.

Chazallon, B., Focsa, C., Charlou, J.L., Bourry, C., Donval, J.P., 2007. A comparative Raman spectroscopic study of natural gas hydrates collected at different geological sites. Chemical Geology 244, 175–185.

Choukroun, M., Morizet, Y., Grasset, O., 2007. Raman study of methane clathrate hydrates under pressure: new evidence for the metastability of structure II. Journal of Raman Spectroscopy 38, 440–451.

Clark, S.H.B., Poole, F.G., Wang, Z., 2004. Comparison of some sediment-hosted, stratiform barite deposits in China, the United States, and India. Ore Geology Reviews 24, 85–101.

Coleman, M.L., Moore, M.P., 1978. Direct reduction of sulfates to sulfur dioxide for isotopic analysis. Analytical Chemistry 50, 1594–1595.

Corsetti, F.A., Grotzinger, J.P., 2005. Origin and significance of tube structure sin Neoproterozoic post-glacial cap carbonates: example from Noonday Dolomite, Death Valley, United States. Palaios 20, 348–362.

Corsetti, F.A., Olcott, A.N., Bakermans, C., 2006. The biotic response to Neoproterozoic snowball Earth? Palaeogeography, Palaeoclimatology, Palaeoecology 232, 114–130.

Crockford, P.W., Wing, B.A., Paytan, A., Hodgskiss, M.S.W., Mayfield, K.K., Hayles, J.A., Middleton, J.E., Ahm, A.S.C., Johnston, D.T., Caxito, F., Uhlein, G., Halverson, G.P., Eickmann, B., Torres, M., Horner, T.J., 2019. Barium-isotopic constraints on the origin of post–Marinoan barites. Earth and Planetary Science Letters 519, 234–244.

Davis, D.W., Lowenstein, T.K., Spencer, R.J., 1990. Melting behavior of fluid inclusions in laboratory-grown halite crystals in the systems NaCl–H_2O, NaCl–KCl–H_2O, NaCl–$MgCl_2$–H_2O, and NaCl–$CaCl_2$–H_2O. Geochimica et Cosmochimica Acta 54, 591–601.

Deynoux, M., Affaton, P., Trompette, R., Villeneuve, M., 2006. Pan-African tectonic evolution and glacial events registered in Neoproterozoic to Cambrian cratonic and foreland basins of West Africa. Journal of African Earth Sciences 46, 397–426.

DiFilippo, E.L., Hammond, D.E., Corsetti, A., 2003. Geochemical constraints for coexisting CO_2 gas hydrate and calcite: implications for sheet cracks, stromatactis, zebra and tepee-like structures. Sedimentary Geology 160, 1–6.

Dornbos, S.Q., Noffke, N., Hagardon, J.W., 2007. Mat-decay structures. In: Schieber, J., Bose, P.K., Eriksson, P.G., Banerjee, S., Sarkar, S., Altermann, W., Catuneanu, O. (Eds.), Atlas of Microbial Mat Features Preserved Within the Siliciclastic Rock Record. Atlases in Geoscience 2. Elsevier, Amsterdam, pp. 106–110.

Dragantis, E., Noffke, N., 2004. Siliciclastic stromatolites and other microbially induced sedimentary structures in an early Devonian barrier-island environment (Muth Formation, NW Himalayas). Journal of Sedimentary Research 74, 191–202.

Frezzotti, M.L., Tecce, F., Casagli, A., 2012. Raman spectroscopy for fluid inclusion analysis. Journal of Geochemical Exploration 112, 1–20.

Gill, F.L., Harding, I.C., Little, C.T.S., Todd, J., 2005. Cenozoic cold seep communities and associated carbonates from the southern Caribbean region. Palaeogeography, Palaeoclimatology, Palaeoecology 227, 191–209.

Goldstein, R.H., Reynolds, T.J., 1994. Systematics of fluid inclusions in diagenetic minerals. SEPM Short Course 31, 1–199.

Gomes, A.S.R., 2005. Modelagem Metalogenética das Mineralizações de Pb-Zn Hospedadas em Carbonatos Neoproterozóicos de Irecê (BA), Serra do Ramalho (BA) e Montalvânia (MG). (PhD)University, Bahia.

Hallmann, C., Kelly, A.E., Gupta, S.N., Summons, R.E., 2011. Reconstructing deep-time biology with molecular fossils. In: Laflamme, M., Schiffbauer, J., Dornbos, S. (Eds.), Quantifying the Evolution of Early Life. Topics in Geobiology 36. Springer, Dordrecht, pp. 355–401.

Halverson, G.P., Hoffman, P.F., Schrag, D.P., Maloof, A.C., Rice, A.H.N., 2005. Toward a Neoproterozoic composite carbon-isotope record. Geological Society of America Bulletin 117, 1181–1207.

Halverson, G.P., Dudás, F.O., Maloof, A.C., Bowring, S.A., 2007. Evolution of the $^{87}Sr/^{86}Sr$ composition of Neoproterozoic seawater. Palaeogeography, Palaeoclimatology, Palaeoecology 256, 103–129.

Han, X., Suess, E., Sahling, H., Wallmann, K., 2004. Fluid venting activity on the Costa Rica margin: new results from authigenic carbonates. International Journal of Earth Sciences 93, 596–611.

Hester, K.C., Dunk, R.M., White, S.N., Brewer, P.G., Peltzer, E.T., Sloan, E.D., 2007. Gas hydrate measurements at Hydrate Ridge using Raman spectroscopy. Geochimica et Cosmochimica Acta 71, 2947–2959.

Hoffman, P.F., 2011. Strange bedfellows: glacial diamictite and cap carbonate from the Marinoan (635 Ma) glaciation in Namibia. Sedimentology 58, 57–119.

Hoffman, P.F., Halverson, G.P., 2011. Neoproterozoic glacial record in the Mackenzie Mountains, northern Canadian Cordillera. In: Arnaud, E., Halverson, G.P., Shields, G. (Eds.), The Geological Record of Neoproterozoic Glaciations. Geological Society, London, Memoirs 36, pp. 397–411.

Hoffman, P.F., Macdonald, F.A., 2010. Sheet-crack cements and early regression in Marinoan (635 Ma) cap dolostones: regional benchmarks of vanishing ice-sheets? Earth and Planetary Science Letters 300, 374–384.

Hoshino, Y., Poshibaeva, A., Meredith, W., Snape, C., Poshibaev, V., Versteegh, G.J.M., Kuznetsov, N., Leider, A., van Maldegem, L., Neumann, M., Naeher, S., Moczydłowska, M., Brocks, J.J., Jarrett, A.J.M., Tang, Q., Xiao, S.H., McKirdy, D., Das, S. K., Álvaro, J.J., Sansjofre, P., Hallmann, C., 2017. Cryogenian evolution of stigmasteroid biosynthesis. Science Advances 3, e1700887.

Hurtgen, M.T., Arthur, M.A., Suits, N.S., Kaufman, A.J., 2002. The sulphur isotopic composition of Neoproterozoic seawater sulphate: implications for a snowball Earth? Earth and Planetary Science Letters 203, 413–429.

Hurtgen, M.T., Arthur, M.A., Prave, A.R., 2004. The sulfur isotope composition of carbonate-associated sulfate in Mesoproterozoic to Neoproterozoic carbonates from Death Valley, California. In: Amend, J.P., Edwards, K.J., Lyons, T.W. (Eds.), Sulphur Biogeochemistry: Past and Present. Geological Society of America, Special Papers 379, pp. 177–194.

Hurtgen, M.T., Arthur, M.A., Halverson, G.P., 2005. Neoproterozoic sulfur isotopes, the evolution of microbial sulfur species, and the burial efficiency of sulphide as sedimentary pyrite. Geology 33, 41–44.

Hurtgen, M.T., Halverson, G.P., Arthur, M.A., Hoffman, P.F., 2006. Sulfur cycling in the aftermath of a 635 Ma snowball glaciation: evidence for a syn-glacial sulfidic deep ocean. Earth and Planetary Science Letters 245, 551–570.

Jewell, P.W., 2000. Bedded barite in the geological record. In: Glenn, C.R., Prévôt-Lucas, L., Lucas, J. (Eds.), Marine Authigenesis: From Global to Microbial. SEPM Special Publications 66, pp. 147–161.

Jiang, G., Kennedy, M.J., Christie-Blick, N., 2003. Stable isotopic evidence for methane seeps in Neoproterozoic postglacial cap carbonates. Nature 426, 822–826.

Jiang, G., Kennedy, M.J., Christie-Blick, N., Wu, H., Zhang, S., 2006a. Stratigraphy, sedimentary structures, and textures of the Late Neoproterozoic Doushantuo cap carbonate in South China. Journal of Sedimentary Research 76, 978–995.

Jiang, G., Shi, X., Zhang, S., 2006b. Methane seeps, methane hydrate destabilization, and the late Neoproterozoic postglacial cap carbonates. Chinese Science Bulletin 51, 1152–1173.

Kennedy, M.J., 1996. Stratigraphy, sedimentology and isotopic geochemistry of Australian Neoproterozoic postglacial cap dolostones: deglaciation, $\delta^{13}C$ excursions and carbonate precipitation. Journal of Sedimentary Research 66, 1050–1064.

Kennedy, M., Mrofka, D., von der Borch, C., 2008. Snowball Earth termination by destabilization of equatorial permafrost methane clathrate. Nature 453, 642–645.

Kesler, S.E., 2005. Ore-forming fluids. Elements 1, 13–18.

Kirschvink, J.L., Raub, T.D., 2003. A methane fuse for the Cambrian explosion: carbon cycles and true polar wander. Comptes Rendus Geoscience 335, 65–87.

Krogh, T.E., 1973. A low contamination method for hydrothermal decomposition of zircon and extraction of U and Pb for isotopic age determination. Geochimica et Cosmochimica Acta 37, 289–297.

Kyle, J.R., Misi, A., 1997. Origin of Zn–Pb–Ag sulfide mineralization within upper Proterozoic phosphate-rich carbonate strata, Irecê basin, Bahia, Brazil. International Geology Review 39, 383–399.

Lahondère, D., Roger, J., Le Metour, J., Donzeu, M., Guillocheau, F., Helm, C., Thieblemont, D., Cochérie, A., Guerrot, C., 2005. Notice Explicative des Cartes Géologiques à 1/200 000 et 1/500 000 de l'extrême Sud de la Mauritanie. DMG, Nouakchott, Rapport BRGM/RC-54273-FR (610 pp.).

Lin, F., Bodnar, R.J., Becker, S.P., 2007. Experimental determination of the Raman CH_4 symmetric stretching (υ_1) band position from 1–650 bar and 0.3–22°C: application to fluid inclusion studies. Geochimica et Cosmochimica Acta 71, 3746–3756.

Luo, G.M., Yang, H., Algeo, T.J., Hallmann, C., Xie, S.C., 2019. Lipid biomarkers for the reconstruction of deep-time environmental conditions. Earth-Science Reviews 189, 99–124.

McMahon, S., van Smeerdijk Hood, A., McIlroy, D., 2016. The origin and occurrence of subaqueous sedimentary cracks. In: Brasier, A.T., McIlroy, D., McLoughlin, N. (Eds.), Earth System Evolution and Early Life: A Celebration of the Work of Martin Brasier. Geological Society, London, Special Publications 448, pp. 285–309.

Misi, A., Iyer, S.S.S., Coelho, C.E.S., Tassinari, C.C.G., Franca-Rocha, W.J.S., de Abreu Cunha, I., Rocha Gomes, A.S., de Oliveira, T.F., Teixeira, J.B.G., Filho, V.M.C., 2005. Sediment hosted lead-zinc deposits of the Neoproterozoic Bambuí Group and correlative sequences, São Francisco Craton, Brazil: a review and a possible metallogenic evolution model. Ore Geol. Rev. 26, 206–304.

Morris, F.K., Grotzinger, J.P., 2023. Facies and stratigraphy of the basal Ediacaran cap carbonate, Naukluft Mountains, Naminia. Precambrian Reseachh 394, 107113.

Nédelec, A., Affaton, P., France-Lanord, C., Charrière, A., Álvaro, J., 2007. Sedimentology and chemostratigraphy of the Bwipe Neoproterozoic cap dolostones (Ghana, Volta Basin): a record of microbial activity in a peritidal environment. Comptes Rendus Geoscience 339, 223–239.

Neunlist, S., Rohmer, M., 1985. Novel hopanoids from the methylotrophic bacteria *Methylococcus capsulatus* and *Methylomonas methanica*. Biochemical Journal 231, 635–639.

Okubo, J., Klyukin, Y.I., Warren, L.V., Sublett Jr., D.M., Bodnar, R.J., Gill, B.C., Xiao, S., 2020. Hydrothermal influence on barite precipitates in the basal Ediacaran Sete Lagoas cap dolostone, São Francisco Craton, Central Brazil. Precambrian Research 340, 105628.

Paula-Santos, G.M., Caetano-Filho, S., Babinski, M., Trindade, R.I.F., Guacaneme, C., 2017. Tracking connection and restriction of West Gondwana São Francisco Basin through isotope chemostratigraphy. Gondwana Research 42, 280–305.

Paytan, A., Mearon, S., Cobb, K., Kastner, M., 2002. Origin of marine barite deposits: Sr and S isotope characterization. Geology 30, 747–750.

Peng, Y., Bao, H., Zhou, C., Yuan, X., 2011. ^{17}O-depleted barite from two Marinoan cap dolostone sections, South China. Earth and Planetary Science Letters 305, 21–31.

Peters, K.E., Moldowan, J.M., 1993. The Biomarker Guide. Interpreting Molecular Fossils in Petroleum and Ancient Sediments. Prentice Hall, New Jersey.

Porter, A.M., Knoll, A.H., Affaton, P., 2004. Chemostratigraphy of Neoproterozoic cap carbonates from the Volta Basin, West Africa. Precambrian Research 130, 99–112.
Pratt, B.R., 2001. Septarian concretions: internal cracking caused by synsedimentary earthquakes. Sedimentology 48, 189–213.
Pratt, B.R., 2002. Tepees in peritidal carbonates: origin via earthquake-induced deformation, with example from the Middle Cambrian of western Canada. Sedimentary Geology 153, 57–64.
Romero, G.R., Mecenero Sánchez, E.A., Morais, L., Boggiani, P.C., Fairchild, T.R., 2016. Tibestone microbialite association in the Ediacaran cap carbonates in the southern Paraguay Fold Belt (SW Brazil): geobiological and stratigraphic implications for a Marinoan cap carbonate. Journal of South American Earth Sciences 71, 172–181.
Rooney, A.D., Selby, D., Houzay, J.P., Renne, P.R., 2010. Re–Os geochronology of a Mesoproterozoic sedimentary succession, Taoudeni basin, Mauritania: implications for basin-wide correlations and Re–Os organic-rich sediment systematics. Earth and Planetary Science Letters 289, 486–496.
Rossi, P., 1982. Lithostratigraphie et Cartographie des Formations Sédimentaires du Pourtour du Massif du Kaarta, Mali Occidental. Travaux du Laboratoire des Sciences de la Terre, St. Jérôme, Marseille, Série B 18 (274 pp.).
Rubinstein, I., Sieskind, O., Albrecht, P., 1975. Rearranged sterenes in a shale: occurrence and simulated formation. Journal of the Chemical Society, Pekin Transactions 1, 1833–1836.
Sato, H., Tahata, M., Sawaki, Y., Maruyama, S., Yoshida, N., Shu, D., Han, J., Li, Y., Komiya, T., 2016. A high-resolution chemostratigraphy of post–Marinoan cap carbonate using drill core samples in the Three Gorges area, South China. Geoscience Frontiers 7, 663–671.
Seifert, W.K., Moldowan, J.M., 1986. Use of biological markers in petroleum exploration. In: Johns, E.B. (Ed.), Methods in Geochemistry and GeophysicsVol. 24. Elsevier, Amsterdam, pp. 26–290.
Shields, G.A., 2007. A normalised seawater strontium isotope curve: possible implications for Neoproterozoic–Cambrian weathering rates and the further oxygenation of the Earth. eEarth 2, 35–42.
Shields, G.A., Kimura, H., Yang, J., Gammon, P., 2004. Sulphur isotopic evolution of Neoproterozoic–Cambrian seawater: new francolite-bound sulphate $\delta^{34}S$ data and critical appraisal of the existing record. Chemical Geology 204, 163–182.
Shields, G.A., Deynoux, M., Strauss, H., Paquet, H., Nahon, D., 2007a. Barite-bearing cap dolostones of the Taoudéni basin, Northwest Africa: sedimentary and isotopic evidence for methane seepage after a Neoproterozoic glaciation. Precambrian Research 153, 209–235.
Shields, G.A., Deynoux, M., Culver, S.J., Brasier, M.D., Affaton, P., Vandamme, D., 2007b. Neoproterozoic glaciomarine and cap dolostone facies of the southwestern Taoudéni Basin (Walidiala Valley, Senegal/Guinea, NW Africa). Comptes Rendus Geoscience 339, 186–199.
Sieskind, O., Joly, G., Albrecht, P., 1979. Simulation of the geochemical transformations of sterols: superacid effect of clay minerals. Geochimica et Cosmochimica Acta 43, 1675–1679.
Sinninghe Damsté, J.S., Kenig, F., Koopmans, M.P., Köster, J., Schouten, S., Hayes, J.M., de Leeuw, J.W., 1995. Evidence for gammacerane as an indicator of water column stratification. Geochimica et Cosmochimica Acta 59, 1895–1900.
Ten Haven, H.L., de Leeuw, J.W., Rullkötter, J., Sinninghe Damsté, J.S., 1987. Restricted utility of the pristane/phytane ratio as a palaeoenvironmental indicator. Nature 330, 641–643.
Ten Haven, H., Rullkötter, J., De Leeuw, J., Sinninghe Damsté, J.S., 1988. Pristane/phytane ratio as environmental indicator. Nature 333, 604.
Torres, M.E., Bohrmann, G., Dubé, T.E., Poole, F.G., 2003. Formation of modern and Paleozoic barite at continental margin methane seeps. Geology 31, 897–900.
Uchida, T., Okabe, R., Mae, S., Ebinuma, T., Narita, H., 2000. *In situ* observations of methane hydrate formation mechanisms by Raman Spectroscopy. Annals of the New York Academy of Sciences 912, 593–601.
Van Kaam-Peters, H.M.E., Rijpstra, W.I.C., de Leeuw, J.W., Sinningue-Damsté, J.S., 1998a. A high resolution biomarker study of different lithofacies of organic sulfur-rich carbonate rocks of a Kimmeridgian lagoon (French southern Jura). Organic Geochemistry 28, 151–177.
Van Kaam-Peters, H., Köster, J., van der Gaast, S.J., Dekker, M., de Leeuw, J.W., Sinninghe Damsté, J.S., 1998b. The effect of clay minerals on diasterane/sterane ratios. Geochimica et Cosmochimica Acta 62, 2923–2929.
Van Maldegem, L.M., Sansjofre, P., Weijers, J.W.H., Wolkenstein, K., Strother, P.K., Wörmer, L., Hefter, J., Nettersheim, B.J., Hishino, Y., Schouten, S., Sinninghe Damsté, J.S., Nath, N., Griesinger, C., Kuznetsov, N.B., Elie, M., Elvert, M., Tegelaar, E., Gleixner, G., Hallmann, C., 2019. Bisnorgammacerane traces predatory pressure and the persistent rise of algal ecosystems after Snowball Earth. Nature Communications 10, 476.
Villeneuve, M., 2005. Paleozoic basins in West Africa and the Mauritanide thrust belt. Journal of African Earth Sciences 43, 166–195.
Villeneuve, M., 2008. Review of the orogenic belts on the western side of the West African craton: the Bassarides, Rokelides and Mauritanides. In: Ennih, N., Liégeois, J.P. (Eds.), The Boundaries of the West African Craton. Geological Society, London, Special Publications 297, pp. 169–202.
Walter, M.R., Veevers, J.J., Calver, C.R., Gorjan, P., Hill, A.C., 2000. Dating the 840–544 Ma Neoproterozoic interval by isotopes of strontium, carbon, and sulfur in seawater, and some interpretative models. Precambrian Research 100, 371–433.
Wang, J., Jiang, G., Xiao, S., Li, Q., Wei, Q., 2008. Carbon isotope evidence for widespread methane seeps in the ca. 635 Ma Doushantuo cap carbonate in South China. Geology 36, 347–350.
Waples, D.W., Machihara, T., 1991. Biomarkers for Geologists. American Association of Petroleum Geologists, Methods in Exploration Series9 pp. 1–91.
Warren, J., 2000. Dolomite: occurrence, evolution and economically important associations. Earth-Science Reviews 52, 1–81.
Zhao, Z., Shen, B., Zhu, J.M., Lang, X., Wu, G., Tan, D., Pei, H., Huang, T., Ning, M., Ma, H., 2021. Active methanogenesis during the melting of Marinoan snowball Earth. Nature Communications 12, 955.
Zundel, M., Rohmer, M., 1985. Hopanoids of the methylotrophic bacteria *Methylococcus capsulatus* and *Methylomonas* sp. as possible precursors for the C29 and C30 hopanoid chemical fossils. FEMS Microbiology Letters 28, 61–64.